JGR Oceans

RESEARCH ARTICLE
10.1029/2020JC016556

Revisit the Vertical Structure of the Eddies and Eddy-Induced Transport in the Leeuwin Current System

Yinghui He[1,3], Ming Feng[2], Jieshuo Xie[1,3], Qingyou He[1,3], Junliang Liu[1,3], Jiexin Xu[1,3], Zhiwu Chen[1,3], Ying Zhang[1,3], and Shuqun Cai[1,3,4]

[1]State Key Laboratory of Tropical Oceanography, South China Sea Institute of Oceanology, CAS, Guangzhou, China, [2]CSIRO Oceans and Atmosphere, Crawley, WA, Australia, [3]Southern Marine Science and Engineering Guangdong Laboratory (Guangzhou), Guangzhou, China, [4]University of Chinese Academy of Sciences, Beijing, China

Key Points:

- A new method for eddy reconstruction is devised that expresses the eddy interior anomaly as eddy-induced and background parts
- Cyclonic (anticyclonic) eddies in the Leeuwin Current system are usually subsurface (surface)-intensified
- The horizontal and vertical structure of volume, heat, and salt transport by the Leeuwin Current system eddies are estimated

Supporting Information:

Supporting Information may be found in the online version of this article.

Correspondence to:

S. Cai,
caisq@scsio.ac.cn

Citation:

He, Y., Feng, M., Xie, J., He, Q., Liu, J., Xu, J., et al. (2021). Revisit the vertical structure of the eddies and eddy-induced transport in the Leeuwin Current system. *Journal of Geophysical Research: Oceans*, *126*, e2020JC016556. https://doi.org/10.1029/2020JC016556

Received 30 JUN 2020
Accepted 21 MAR 2021

Abstract The vertical structure of eddies in the Leeuwin Current system affects the eddy volume, heat, and salt transport, even the ecosystem. However, the understanding of eddy vertical structure and eddy-induced transport here are still very limited. In this study, satellite observed sea surface heights were combined with decade-long in situ measurements of Argo floats to study the vertical structure of mesoscale eddies in the LC system and their volume, heat, and salt transport. A novel eddy reconstruction method, which considers the influences of both the eddy and background flow, is devised to study the three-dimensional structure of eddies. Result shows that, in LC system, anticyclonic eddies (AEs) are usually surface-intensified, with the geostrophic velocity decreasing sharply below the mixed layer, while cyclonic eddies (CEs) are subsurface-intensified, with a maximum speed at 240 m. The density anomaly core of the average AE (CE) is at a depth of 130 m (650 m) with a density anomaly of −0.51 (0.24) kg/m^3. The volume-integrated eddy kinetic energy and available potential energy of the average CE are much larger than those of the average AE. The average lifespan of CEs is significantly longer than that of AEs, which can be explained by the deeper vertical scale of CEs. The offshore volume transport by eddy drift across the coastal (107°E) section is 9.05 Sv (12.5 Sv). The heat and salt onshore transport by eddy drift across the coastal (107°E) section are, respectively, 10.6 Tw and 143.1 ton/s (17.1 Tw and 241.0 ton/s).

Plain Language Summary Mesoscale eddies are ubiquitous in the ocean; their surface characteristics can be well observed by satellite altimetry, but most of their interior information is currently unclear. To understand the vertical structure of an eddy, previously, oceanographers have composited eddies based on satellite altimeter and Argo profile data. The present work has improved upon this method and associates the interior anomaly of an eddy with its surface amplitude and edge height. When we applied this method to the study of eddies off Western Australia, we found that the vertical structures of cyclonic eddies (CEs) and anticyclonic eddies (AEs) in this region are very different. In general, CEs are more energetic, have longer lifespans, and propagate farther than AEs, which could play a more important role in water mass redistribution and heat transport in the southeastern Indian Ocean.

1. Introduction

1.1. Circulation and Eddies in the Leeuwin Current System

The circulation of the eastern boundary of the south Indian Ocean (SIO) (Figure 1) is dominated by Leeuwin Current (LC) system, that is, the poleward-flowing LC in the upper layer (shallower than 300 m), which transport warm and the fresh water of tropical origin (Feng et al., 2003), and equatorward-flowing Leeuwin Undercurrent (LUC) in the lower layer (300–800 m), which transport the Sub-Antarctic Mode Water (SAMW) from south of Australia (Talley et al., 2011). It is unique that the poleward-flowing eastern boundary current is above the equatorward-flowing current, which is opposite to the other major eastern boundary current system. In the interior SIO, the upper ocean (shallower than 300 m) is dominated by eastward flows, which tend to split into serval jets, while the subsurface (deeper than 300 m) is dominated by westward flows (Menezes et al., 2014). A large fraction of the upper layer eastward flow from the interior SIO enters the LC, sinks into the LUC, and then exits as the westward subsurface flow, forming a zonal overturning circulation (Furue et al., 2017).

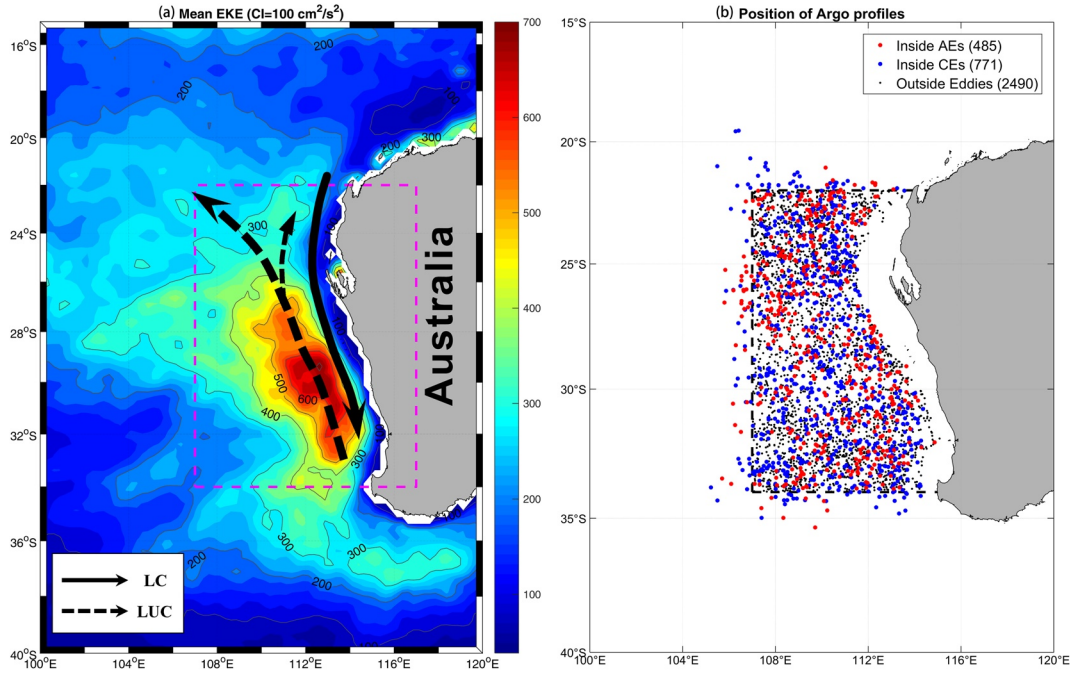

Figure 1. Eddy kinetic energy (unit: cm^2/s^2) and position of Argo profiles in the eastern boundary of the South Indian Ocean. (a) The solid arrow denotes the Leeuwin Current, while the dashed arrows denote the Leeuwin Undercurrent. The box with the magenta frame denotes the region we studied. (b) Red and blue and dots denote 485 and 771 Argo profiles inside AEs and CEs, respectively. Black dots denote 2,490 profiles outside eddies. Note that some profiles outside the study box (denoted by black dashed line) are used because they are inside the eddies which are centered in the study box. AE, anticyclonic eddies; CE, cyclonic eddies.

Due to the mixed barotropic/baroclinic instability of the mean current (Feng et al., 2005; Pearce & Griffiths, 1991; Rennie et al., 2007; Zheng et al., 2015), mesoscale eddies are generated from the LC system, where the strongest eddy kinetic energy (EKE) among all the midlatitude eastern boundary current is observed. Both the LC transport and regional EKE have a significant seasonal cycle, which is stronger in the austral winter (Feng et al., 2003). Their interannual variability is dominated by the ENSO cycle. They are stronger in La Niña years and weaker in El Niño years (Zheng et al., 2018).

1.2. Vertical Structure of Eddies

The vertical structures of eddies are crucial for estimating the physical, chemical, and biological property transport by eddies. Oceanic eddies can be classified as surface-intensified and subsurface-intensified types according to the vertical position of the potential vorticity (PV) core, where PV reaches its maximum (Assassi et al., 2016). The surface-intensified eddies are characterized by their maximum geostrophic velocity at or near the surface, whose density and temperature core are generally within the thermocline. Due to their clear surface signature, most the eddies observed by satellites are surface-intensified types (Capet et al., 2013; Z. Zhang et al., 2013). In contrast, the subsurface-intensified eddies are characterized by their maximum geostrophic velocity in the subsurface. According to the vertical position of their density or temperature core, where their density or temperature anomaly reaches a maximum, they are also called intrathermocline eddies (Hormazabal et al., 2013) or subthermocline eddies (Pelland et al., 2013).

Subsurface-intensified eddies have been observed in various sites of the World Ocean. Such as the Mediterranean water eddies in the northeastern Atlantic (Barceló-Llull et al., 2017), the California Undercurrent eddies in the northeastern Pacific (Cornuelle et al., 2000), the subsurface-intensified AEs in the southeastern Pacific (Hormazabal et al., 2013), The Kuroshio Extension intermediate-layer eddies in the northwestern Pacific (Z. Zhang et al., 2015). Subsurface-intensified eddies commonly have a deeper vertical extent, and therefore are thought to have more capacity to transport mass, heat and salt when comparing with

the surface-intensified eddies. Previous studies have shown that they play an important role in the distribution of the thermohaline properties and the nutrient transport (Barceló-Llull et al., 2017; Dilmahamod et al., 2018; Hormazabal et al., 2013; McGillicuddy et al., 2007).

1.3. Eddy Composite Methods

The surface characteristics of oceanic eddies can be effectively acquired by the satellite altimeter data (e.g., Chelton et al., 2011). The Argo floats are often combined with the satellite altimeter data to study the eddy vertical structure. Chaigneau et al. (2011) first used eddy composite analysis to study the vertical structure of eddies in the eastern South Pacific Ocean. With modifications by the following researchers, this method has been widely applied in the global or regional ocean to obtain the vertical structure of eddies and further estimate eddy-induced heat and salt transport (e.g., Amores et al., 2017; Dong et al., 2017; Gulakaram et al., 2020; B. Sun et al., 2019). However, this composite method does not normalize the eddy amplitude. When eddies with different amplitudes are composited to one eddy, the temperature and salinity anomalies in the composite eddy would be oversmoothed.

Z. Zhang et al. (2013) proposed a universal eddy vertical structure, then the pressure anomaly in an eddy can be reconstructed as the product of eddy amplitude and the universal eddy vertical mode. Based on this method, Z. Zhang et al. (2014) estimated the volume transport by global oceanic eddies. However, this universal structure does not distinguish the different structures between the CE and AE. Moreover, other processes, such as large-scale background flows or internal waves, could strongly influence the vertical profile as well as the eddy (Keppler et al., 2018). None of the previous eddy composite methods considered the effect of background flows.

1.4. Significance and Objectives of This Study

Eddies play a vital role in the physical and ecosystem function of the LC system (Guo, Li, Wang, Wei, & Xia, 2020; Waite et al., 2007). For example, eddies contribute alongshore momentum balance of the LC and modulate the transport of Indonesian Throughflow (Feng et al., 2005). Eddies transport heat and salt offshore, impacting the temperature and salinity in the South Indian Ocean (Dilmahamod et al., 2018; Domingues et al., 2006; Guo, Li, Wang, Wei, & Rong, 2020; Qu et al., 2019). Eddies affect the distribution of chlorophyll in the South Indian Ocean through entrainment and mixed layer processes (Dufois et al., 2014). To better estimate the eddy-induced transport and its biological effects, it is necessary to understand the eddy vertical structure.

The vertical structures of eddies in the LC system have been researched by several case studies based on shipboard investigations (e.g., Feng et al., 2007; Fieux et al., 2005; Mao et al., 2018). Morrow et al. (2003) investigated three warm eddies with a high positive sea level anomaly (SLA) and found that these eddies are surface intensified and penetrated to at least 1,500 m depth. Both Feng et al. (2007) and Mao et al. (2018) investigated two counter-rotating eddy pairs off Western Australia. Coincidentally, both the AEs have strong baroclinic structures, while the two CEs have barotropic structures in the upper 500 m. It is still unclear whether the CEs can also penetrate to a deep depth.

Limited by the scarce spatial coverage and short-duration of the shipboard observations, the vertical structures of eddies in the LC system are largely unknown. Moreover, previous studies on the eddy-induced transport in the LC system are limited to the heat transport by eddy stirring based on numerical model results (e.g., Domingues et al., 2006), but the quantitative estimation based on in-situ observations and studies on the volume, heat and salt transports by eddy movement is still very few. Hence, the main objective of the present study is to understand the vertical structure of eddies in the LC system and quantify their volume, heat, and salt transports using long-term and widely covered satellite and Argo profile data.

The paper is organized as follows. In Section 2, we describe the satellite and Argo data used in this study and briefly present the eddy identification and tracking algorithms. We propose a new eddy composite method that considers the effects of background flow and eddies on the density, temperature, and salt anomalies in this section. The statistics of eddy horizontal property, eddy vertical structure, eddy energy, and eddy-induced volume, heat, and salt transport are described in Section 3. In Section 4, we summarize the results

and discussed the reason why there are distinct vertical structures between CEs and AEs. The accuracy of the eddy reconstruction method is also discussed in Section 4.

2. Data and Methods

2.1. Satellite Data and Argo Profiles

The altimetry data are provided by the Archiving, Validation, and Interpretation of Satellite Oceanographic (AVISO). These data have daily values covering the period from January 1993 to December 2016 on a 0.25 ° × 0.25 ° grid. The "all sat merged" data used all missions available at a given time which is consisted of datasets with up to four satellites at a given time. The reference period of the SLA is based on a 20-year period data from 1993 to 2012. The SLA data were smoothed with a low-pass filter of 0.75 ° × 0.75 ° to reduce noise in this study.

Sea surface temperature (SST) data are from the NOAA 1/4° daily Optimum Interpolation SST (OISST) v2.0, which are constructed by combining observations from different platforms, such as satellites, ships, and buoys. We use the AVHRR-only OISST data, which has a temporal coverage from 1993 to 2016. The time average SST from 1993 to 2012, which is consistent with the reference period of the SLA, is removed to get SST anomaly (SSTA).

Delayed-mode Argo data profiles from January 2000 to December 2016 are provided by the Coriolis Global Data Acquisition Center of France through the website ftp://ftp.ifremer.fr/ifremer/argo/geo/. These profiles have undergone automatic preprocessing and quality control procedures by the Argo data center. Following previous studies (e.g., Chaigneau et al., 2011; Pegliasco et al., 2015; W. Sun et al., 2017; Yang et al., 2013), only the Argo profile data meeting the following standards are used in the further analysis:

1. The quality flag of pressure, temperature, and salinity data are good (Argo quality flag 1 or 2)
2. Only profiles with the shallowest observation depth are shallower than 10 m and the deepest observation depth are deeper than 1,000 m are selected
3. The depth difference between two consecutive records must not exceed a given limit (Δz), which depends on depth range (Δz = 25 m for the 0–100 m layer, Δz = 50 m for the 100–300 m layer, Δz = 100m for the 300–1,000 m layer)
4. Based on all the requirements mentioned above, the number of data levels in each profile must no less than 30

2.2. Eddy Identification and Tracking

An eddy is a simply connected region surrounded by its periphery which is defined as the outmost closed SLA contour line and satisfies the following criteria,

1. All SLA values within the eddy are above or below the SLA value of the outmost contour for AEs and CEs, respectively
2. The area within the eddy is larger than four grids of equivalent area
3. There is at least one local maximum or minimum of SLA for AEs and CEs, respectively. The center of an AE or CE is the point with the maximum or minimum of SLA within the outermost contour, respectively, and must be over water deeper than 200 meters
4. The distance between any pair of points within the connected region must be less than 4°
5. The eddy shape error which is defined as the ratio between the sum of the total area of deviations from the circle to the area of the circle (Kurian et al., 2011) is no more than 50%

The criteria 1 to 4 are adapted from Chelton et al. (2011) and have been successfully used in the marginal seas (He et al., 2016, 2017). Criterion 5 is introduced as an eddy shape error judgment following Kurian et al. (2011). Compared with Chelton et al. (2011) and Faghmous et al. (2015) eddy data set, this criterion can effectively reduce detecting bogus eddies (e.g., filaments or irregular eddy edge).

The eddy tracking algorithm is an adaption of that used by Chaigneau et al. (2008). First, for each eddy (e_1) identified on a given map at time t_1 for each eddy (e_2) identified on another map at time t_2 with the same polarity, a non-dimensional distance is defined as follows:

$$D_{e_1,e_1} = \sqrt{\left(\frac{\Delta D}{D_0}\right)^2 + \left(\frac{\Delta R}{R_0}\right)^2 + \left(\frac{\Delta \zeta}{\zeta_0}\right)^2 + \left(\frac{\Delta \mathrm{EKE}}{\mathrm{EKE}_0}\right)^2}, \quad (1)$$

where ΔD is the smallest one of ΔD_1 and ΔD_2. Here ΔD_1 is the distance between the centers of e_1 and e_2, and ΔD_2 is the distance between the centroids of e_1 and e_2. ΔR is the radius variation between e_1 and e_2. D_0, R_0, ζ_0, and EKE_0 are, respectively, the characteristic length scale ($D_0 = 100$ km), characteristic radius ($R_0 = 50$ km), characteristic vorticity ($\zeta_0 = 10^{-6}\mathrm{s}^{-1}$) and characteristic EKE ($\mathrm{EKE}_0 = 100\ \mathrm{cm}^2\mathrm{s}^{-2}$). Then, the algorithm selects the eddy pair (e_1, e_2) that minimizes $D_{e1,\,e2}$ at consecutive times t_1 and t_2 and considers this pair to be the same eddy that is tracked from t_1 to t_2. The distance ΔD of the eddy pair (e_1, e_2) must be less than 150 km. Then, for the remaining unpaired eddies, we repeat this algorithm for a time interval of 2 days (i.e., the time interval from t_1 to t_2 equals 2 days) to minimize the problem of eddies disappearing when they pass into the gaps between satellite ground tracks.

2.3. Relationship of Underwater Density, Temperature, and Salinity With SSH

The circulation in the eastern boundary of SIO has significant interannual and seasonal variations (Feng et al., 2003; Furue et al., 2017; Menezes et al., 2016), leading to the corresponding regional SSH and sea water density anomalies. The instability of the background currents generates abundant eddies, which further changes the local SSH and density. To reconstruct the eddy structure, we should distinguish the background and eddy-induced parts in the observed SSH and density anomalies since the formation mechanism and vertical structure of the two parts are different.

First, we decompose SSH η as follows,

$$\eta = \bar{\eta} + \eta' = \bar{\eta} + \eta'_{\mathrm{eddy}} + \eta'_{\mathrm{bg}} \quad (2)$$

where $\bar{\eta}$ is climatological mean SSH, η' is the SSH anomaly (SSHA), which is composed of eddy-induced SSHA η'_{eddy} and background part η'_{bg}. The background part contains interannual and seasonal variations of SSHA. In this study, $\bar{\eta}$ is mean dynamic topography, η' is the SLA from the altimetry data. The eddy edge is the boundary that separates the eddy interior against the background circulation, so we specify the eddy edge height as the background SSHA η'_{bg}. Thus, the eddy-induced SSHA η'_{eddy} can be calculated by $\eta' - \eta'_{\mathrm{bg}}$. In this sense, η'_{bg} is uniform in an eddy, but η'_{eddy} depends on the eddy amplitude and the distance from the eddy center.

Similarly, the density, temperature, and salinity variations can also be decomposed as,

$$\rho = \bar{\rho} + \rho' = \bar{\rho} + \rho'_{\mathrm{eddy}} + \rho'_{\mathrm{bg}} \quad (3)$$

$$T = \bar{T} + T' = \bar{T} + T'_{\mathrm{eddy}} + T'_{\mathrm{bg}} \quad (4)$$

$$S = \bar{S} + S' = \bar{S} + S'_{\mathrm{eddy}} + S'_{\mathrm{bg}} \quad (5)$$

Since SSHA is observed by satellite altimetry, if we can find the relationship of the eddy-induced and background SSHA with the corresponding parts of the density, temperature, and salinity anomaly, the eddy vertical structure can be derived.

Mesoscale processes satisfy quasi-geostrophic dynamics (Cushman & Backers, 2011). The eddy-induced pressure anomaly p'_{eddy}, density anomaly ρ'_{eddy}, and stream function ψ satisfy the following relationship,

$$p'_{\mathrm{eddy}}(x,y,z,t) = \rho_0 f_0 \psi(x,y,z,t) \quad (6)$$

$$\rho'_{\mathrm{eddy}}(x,y,z,t) = -\frac{\rho_0 f_0}{g} \cdot \frac{\partial \psi(x,y,z,t)}{\partial z} \quad (7)$$

Assuming that the stream function ψ can be expressed as the product of a horizontal mode Φ and a vertical mode H,

$$\psi(x,y,z,t) = \phi(x,y,t) \cdot H(z) \tag{8}$$

This assumption has been applied in many previous eddy studies (e.g., Flierl, 1987; Z. Zhang et al., 2013).

At the surface, we have,

$$p'_{\text{eddy}}(x,y,0,t) = \rho_0 f_0 \cdot \phi(x,y,t) \cdot H(0) = \rho_0 g \eta'_{\text{eddy}}(x,y,t) \tag{9}$$

Let $H(0) = 1$, from Equations 6–9, it yields,

$$\phi(x,y,t) = \frac{g}{f_0} \cdot \eta'_{\text{eddy}}(x,y,t) \tag{10}$$

$$\rho'_{\text{eddy}}(x,y,z,t) = \alpha_\rho(z) \cdot \eta'_{\text{eddy}}(x,y,t), \tag{11}$$

where α_ρ is defined as,

$$\alpha_\rho(z) = -\rho_0 \cdot \frac{dH(z)}{dz} \tag{12}$$

Here, the coefficient α_ρ is introduced to bridge the density anomaly ρ'_{eddy} and the eddy-induced SSHA η'_{eddy}. Hereinafter, α_ρ is called the eddy-induced reconstruction coefficient (EIRC) of density. Since the relationship between the background SSHA and density anomaly is still unknown, similar to the eddy-induced part, we also assume the background density anomaly as a linear function of the background SSHA,

$$\rho'_{\text{bg}}(x,y,z,t) = \beta_\rho(z) \cdot \eta'_{\text{bg}}(x,y,t) + \varepsilon_\rho(x,y,z,t) \tag{13}$$

where ε_ρ is the bias due to nonlinearity and random error. Equation 12 shows that the EIRC of density α_ρ is deduced from the vertical mode of eddy $H(z)$. Therefore, the background reconstruction coefficient (BGRC) of density β_ρ is also associated with the vertical mode of background flow. Equations 3, 11 and 13 yield,

$$\rho'(x,y,z,t) = \alpha_\rho(z) \cdot \eta'_{\text{eddy}}(x,y,t) + \beta_\rho(z) \cdot \eta'_{\text{bg}}(x,y,t) + C_\rho(z) + \varepsilon_\rho(x,y,z,t) \tag{14}$$

a constant term C_ρ is included which represents the density anomalies that cannot be interpreted by the η'_{eddy} and η'_{bg}. Note that C_ρ cannot be explained by the QG dynamics and maybe come from the processing of the satellite data (Castelao, 2014).

A previous study indicates that the eddy SSHA is linearly correlated with the subsurface temperature and salinity anomalies (Castelao, 2014). Similar as Equation 14, we also express the temperature and salinity anomaly as a linear combination of the eddy-induced and background SSHA:

$$T'(x,y,z,t) = \alpha_T(z) \cdot \eta'_{\text{eddy}}(x,y,t) + \beta_T(z) \cdot \eta'_{\text{bg}}(x,y,t) + C_T(z) + \varepsilon_T(x,y,z,t) \tag{15}$$

$$S'(x,y,z,t) = \alpha_S(z) \cdot \eta'_{\text{eddy}}(x,y,t) + \beta_S(z) \cdot \eta'_{\text{bg}}(x,y,t) + C_S(z) + \varepsilon_S(x,y,z,t) \tag{16}$$

2.4. Reconstruction of the Eddy Vertical Structure

First, using daily resolution satellite altimeter SLA data from January 1993 to December 2016, eddies in the south Indian Ocean are identified and tracked. Eddies centered in the LC system (107°E~117°E, 34°S~22°S) and with lifespan over 28 days are kept for further analysis. Secondary, Argo profiles surfaced into those eddies on the same day are selected and quality controlled. Then the observed temperature (T), salinity (S), and density (ρ) are interpolated onto 150 regularly spaced vertical levels every 10 m from 10 to 1,500 m.

Table 1
Eddy Properties Statistics

Eddy polarity	Cyclonic eddies					Anticyclonic eddies				
Season	Annual	Spring (Sep–Nov)	Summer (Dec–Feb)	Autumn (Mar–May)	Winter (Jun–Aug)	Annual	Spring (Sep–Nov)	Summer (Dec–Feb)	Autumn (Mar–May)	Winter (Jun–Aug)
No. realizations	50,763	13,466	11,772	12,086	13,439	35,666	9,373	8,930	8,489	8,874
No. eddies	630	135	140	160	195	573	162	126	134	151
Radius (km)	77.47	79.26	77.59	76.54	76.42	81.37	83.31	81.36	77.34	83.19
Center height (cm)	−11.78	−16.69	−12.86	−7.08	−10.15	23.01	21.50	18.68	23.21	28.76
Amplitude (cm)	−10.61	12.93	9.65	8.22	11.29	10.96	12.31	9.71	8.75	12.90
Edge height (cm)	−1.17	−3.77	−3.21	1.13	1.15	12.05	9.19	8.97	14.46	15.86
Maximal circum-average speed (cm/s)	34.31	39.95	30.62	27.58	37.96	33.16	35.86	28.96	28.70	38.79
Lifespan (day)	137.54	154.76	119.85	131.63	143.16	84.58	92.65	67.96	80.87	93.07
Displacement (km)	403.97	468.97	354.81	367.76	423.98	276.75	301.61	201.98	237.69	347.15
Propagation speed(cm/s)	6.43	6.33	6.53	6.42	6.44	6.39	6.10	6.15	6.43	6.87

Notes. The number of eddy realizations is the total number from 1999 to 2016. The number of eddies is the eddies generated in the study area (Figure 1) from 1999 to 2016. The radius, center height, amplitude, edge height, and maximal circum-average speed are averaged for each eddy realization, while the lifespan and displacement are averaged for each eddy track.

Over the entire study period, we obtained a total of 771 profiles inside CEs, 485 inside AEs (Figure 1b). This proportion is in agreement with the ratio of the identified number of CE to AE realizations (Table 1). The anomalies of every property (T', S', ρ') are computed by removing climatological profiles, which are obtained by interpolating the World Ocean Atlas 2013 data (Locarnini et al., 2013; Zweng et al., 2013) to positions of Argo profiles. Third, we calculated the background and eddy-induced SSHA of the Argo profiles. The SSHA above the Argo profiles (η') is obtained by interpolating the satellite SLA to positions and times of profiles. The background SSHA (η'_{bg}) of each profile is the edge height of the eddy where this profile is located. The eddy-induced SSHA (η'_{eddy}) of each profile is calculated as η' minus η'_{bg}. Fourthly, using $T', S', \rho', \eta'_{\mathrm{bg}}, \eta'_{\mathrm{eddy}}$ Argo profiles inside CEs and AEs, respectively, the reconstruction coefficients of density, temperature, and salinity $(\alpha_\chi, \beta_\chi, C_\chi)$ of CEs and AEs can be estimated by least-squares according to Equations 14–16, where χ is either ρ, T or S. The optimal parameters $(\alpha_\chi, \beta_\chi, C_\chi)$ are sought to minimize the square norm of the error ε_χ in Equations 14–16, where the norm is defined using all samples in CEs or AEs. Finally, for any eddy detected in the first step, we can decompose the SSHA inside the eddy to η'_{bg} and η'_{eddy}, and then reconstruct the eddy density, temperature, and salinity anomalies by:

$$\widehat{\rho'}(x,y,z,t) = \alpha_\rho(z)\cdot\eta'_{\mathrm{eddy}}(x,y,t) + \beta_\rho(z)\cdot\eta'_{\mathrm{bg}}(x,y,t) + C_\rho(z) \tag{17}$$

$$\widehat{T'}(x,y,z,t) = \alpha_T(z)\cdot\eta'_{\mathrm{eddy}}(x,y,t) + \beta_T(z)\cdot\eta'_{\mathrm{bg}}(x,y,t) + C_T(z) \tag{18}$$

$$\widehat{S'}(x,y,z,t) = \alpha_S(z)\cdot\eta'_{\mathrm{eddy}}(x,y,t) + \beta_S(z)\cdot\eta'_{\mathrm{bg}}(x,y,t) + C_S(z) \tag{19}$$

2.5. Regional Average CE and AE

To illustrate the average vertical structure of CEs and AEs, two ideal Gaussian eddies with the regionally averaged radius, edge height, and amplitude of the CEs and AEs are constructed, respectively. Hereinafter, these two eddies are referred to as the average CE and AE, respectively.

The SSHA of an idea Gaussian eddy with amplitude of A, the radius of R and edge height of η'_{bg} is

$$\eta' = \frac{A \cdot e}{e-1} \cdot e^{-\frac{r^2}{R^2}} + \eta'_{\mathrm{bg}} - \frac{A}{e-1} \tag{20}$$

where r is the radial distance to the eddy center, e is the base of the natural logarithm. A is the eddy amplitude, which is defined as the SLA difference between eddy center and eddy edge. R is the eddy radius, which corresponds to the radius of a circle with an area equal to that within the eddy edge. Parameters of the average CE (Table 1): $A = -10.61$ cm, $R = 77.47$ km, η'_{bg} = -1.17 cm; parameters of the average AE (Table 1): $A = 10.96$ cm, $R = 81.37$ km, $\eta'_{\mathrm{bg}} = 12.05$ cm. Then, the density, temperature, and salinity anomalies in the average eddies are reconstructed by Equations 17–19.

2.6. Geostrophic Velocities

Since the background SSHA η'_{bg} is uniform in an eddy,

$$\frac{\partial \eta'_{\mathrm{bg}}}{\partial x} = \frac{\partial \eta'_{\mathrm{bg}}}{\partial y} = 0, \tag{21}$$

the thermal wind balance yields,

$$\frac{\partial u_g}{\partial z} = \frac{g}{f\rho_0} \cdot \frac{\partial \rho'}{\partial y} = \frac{g\alpha_\rho}{f\rho_0} \cdot \frac{\partial \eta'}{\partial y} \tag{22}$$

$$\frac{\partial v_g}{\partial z} = -\frac{g}{f\rho_0} \cdot \frac{\partial \rho'}{\partial x} = -\frac{g\alpha_\rho}{f\rho_0} \cdot \frac{\partial \eta'}{\partial x} \tag{23}$$

where u_g and v_g are the zonal and meridional components of geostrophic velocities in the eddy, respectively. Geostrophic velocities at depth z_0 are calculated as follows:

$$u_g(z) = \frac{g}{f\rho_0} \cdot \frac{\partial \eta'}{\partial y} \cdot \int_{z_{\mathrm{ref}}}^{z} \alpha_\rho dz' \tag{24}$$

$$v_g(z) = -\frac{g}{f\rho_0} \cdot \frac{\partial \eta'}{\partial x} \cdot \int_{z_{\mathrm{ref}}}^{z} \alpha_\rho dz' \tag{25}$$

where z_{ref} is the reference level, which is set to 1,500 m in this study. The above equations show that the geostrophic velocity in each depth is the product of the surface geostrophic velocities $\left(-\frac{g}{f}\frac{\partial \eta'}{\partial y}, \frac{g}{f}\frac{\partial \eta'}{\partial x}\right)$ and the vertical mode $H(z) = -\frac{1}{\rho_0}\int_{z_{\mathrm{ref}}}^{z} \alpha_\rho dz'$.

2.7. Eddy Kinetic Energy and Available Potential Energy

Based on Equations 11 and 12, the EKE and available potential energy (APE) under quasi-geostrophic dynamics are expressed as (Cushman & Beckers, 2011)

$$\mathrm{EKE} = \frac{1}{2}\rho_0 |\nabla \psi|^2 = \frac{\rho_0 g^2}{2 f_0^2} \cdot \left|\nabla \eta'_{\mathrm{eddy}}\right|^2 H^2, \tag{26}$$

$$\mathrm{APE} = \frac{1}{2}\rho_0 \frac{f_0^2}{N^2}\left(\frac{\partial \psi}{\partial z}\right)^2 = \frac{g^2}{2\rho_0 N^2} \cdot \left(\alpha_\rho \eta'_{\mathrm{eddy}}\right)^2. \tag{27}$$

The area integrated EKE and APE of the average CE (AE) against depth are calculated by the surface integral of Equations 26 and 27 over the region inside the average CE (AE) periphery, respectively. Upon substitution of η'_{eddy} deduced from Equation 20, we obtain

$$K(z) = \int_0^{2\pi} d\theta \int_0^R \text{EKE} \cdot r dr = \frac{\rho_0 g^2}{2} \cdot \pi\left(1 - 3e^{-2}\right) \cdot \frac{A^2 H^2}{{f_0}^2} \tag{28}$$

$$P(z) = \int_0^{2\pi} d\theta \int_0^R \text{APE} \cdot r dr = \frac{g^2}{4\rho_0} \cdot \pi\left(1 - 4e^{-1} + 5e^{-2}\right) \cdot \frac{R^2 A^2 {\alpha_\rho}^2}{N^2} \tag{29}$$

where R is the radius of the average CE or AE.

3. Results

3.1. Eddy Properties From the Satellite Altimetry Data

Eddy properties in the LC system were censused from 1999 to 2016 (Table 1) when the Argo profiles and satellite altimetry data coexist. There is little difference between the number of the CEs (630) and AEs (573). The mean values of the amplitude, radius, and maximal circum-average geostrophic speed of the CEs are 10.61 cm, 77.47 km, and 34.31 cm/s, respectively, which are close to those of the AEs, whose values are 10.96 cm, 81.37 km, and 33.16 cm/s, respectively. However, the mean lifespan of the CEs (137.54 days) is significantly longer than that of the AEs (84.58 days). Consequently, the mean displacement of CEs is significantly farther than that of AEs, with a value of 403.97 versus 276.75 km. The significant difference in the lifespan between CEs and AEs from this region are also found in the eddy data set of and Faghmous et al. (2015) and the Genealogical Evolution Model (Li et al., 2016).

In the seasonal cycle (Table 1), the radius, amplitude, and maximal circum-average geostrophic speed of CEs peak in austral spring, while those of AEs peak in austral winter. The radius, amplitude, and maximal circum-average geostrophic speed of both CEs and AEs reach a minimum in austral autumn. The seasonal cycle of the lifespan and displacement of eddies are basically identical with the amplitude of eddies, which are larger in winter/spring and smaller in summer/autumn. Moreover, the edge height of eddies, that is, the background SSH, is also higher in winter/spring and lower in summer/autumn, corresponding to the seasonal cycle of the regional SSH (Feng et al., 2003).

Chaigneau et al. (2011) found that the eddy lifespan is correlated with eddy amplitude in the eastern South Pacific Ocean. In the LC system, the seasonal variation of eddy lifespan is consistent with that of the eddy amplitude, suggesting that this correlation also applies to CEs or AEs in this region. However, the minor difference of amplitudes between CEs and AEs is not sufficient to cause a significant difference in the lifespan. Therefore, some other factors cause the difference in the lifespans between CEs and AEs.

3.2. Density Anomalies in Eddies

The correlation coefficients between Argo observed and reconstructed density anomalies (Figure 2a) are used to evaluate the effectiveness of the reconstructed results. It shows that the reconstructed values are significantly correlated with the observation data (at a 99% confidence level) at all depths, which indicates our regression model is reliable. The correlation coefficients in AEs are large (>0.7) in the subsurface layer (i.e., 50–370 m), while those in CEs are large below the subsurface layer (i.e., below 400 m). This indicates that AEs and CEs dominate density anomalies in different depth ranges. Those high correlations also indicate that the density anomalies at those depths are mainly caused by the background flow and/or eddy-induced effects. Although the root mean square of error may not be small at depths with high correlations, the error variance as percentages of signal (i.e., density, temperature, or salinity) variance is small there (see Figure S1).

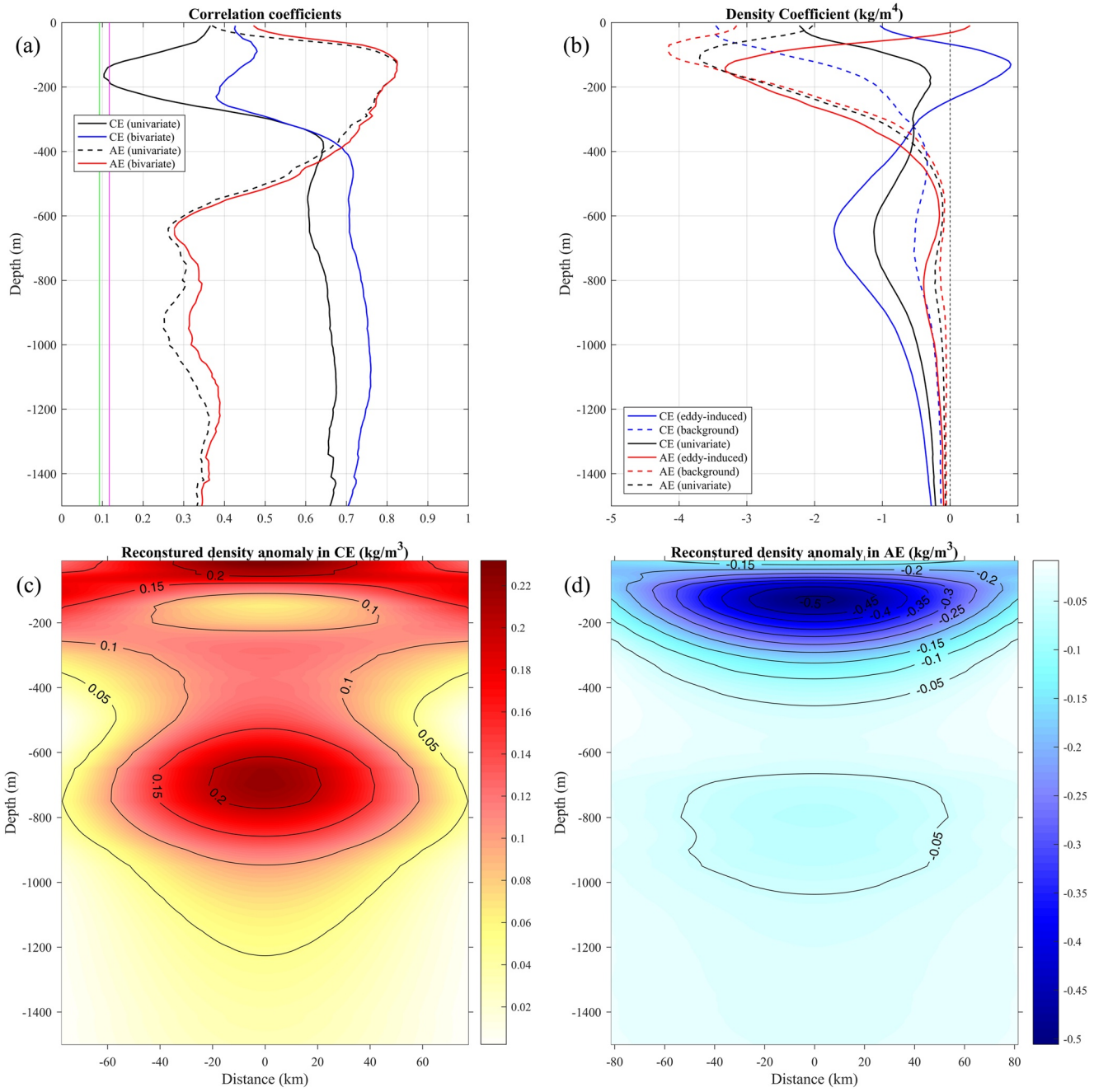

Figure 2. Correlation coefficients of predict density with Argo data, reconstruction coefficients of density, and density anomalies in average CE and AE. (a) Correlation coefficients of predicted density with Argo data. The green (Magenta) line represents a 99% confidence level for CEs (AEs). Univariate and bivariate in the legend, respectively, indicate that one independent variable (i.e., η' in Equation 35) and two independent variables (i.e., η'_{eddy} and η'_{bg} in Equations 17–19) are used in the regression analysis. Blue (red) lines denote the values for CEs (AEs). (b) Reconstruction coefficients of density (unit: cm^2/s^2). Solid (dashed) blue or red lines denote the EIRC (BGRC); Solid (dashed) black lines denote the coefficients of CEs (AEs) without distinguishing the background and eddy-induced effects. (c) Density anomalies (kg/m^3) in the average CE. (d) Density anomalies (kg/m^3) in the average AE. AE, anticyclonic eddies; CE, cyclonic eddies.

At some depths, the correlations are relatively low, where other physical processes, such as surface heating and internal waves, are expected to influence the density anomaly. For example, in the mixed layer (<50 m), both the correlation coefficients (Figure 2a) of CEs and AEs are not large (<0.6) because the density variation in the mixed layer is associated with the surface heating, cooling, evaporation, and precipitation, as well

as the dynamic processes. In addition, low correlations occur in the intermediate and deep layers for AEs, but in the subsurface layer for CEs.

The reconstruction coefficient of density reflects the response of oceanic stratification to the variation of SSH. Here, the BGRC of density indicates the relationship between variations of the background circulation and SSH. The BGRCs of the density of CEs and AEs are always negative, which is consistent with the expectation given by the reduced-gravity model. That is, when the SSH rises, perhaps due to the intensification of the subtropical gyre or boundary currents, the pycnocline depth will deepen, leading to a negative density anomaly, and vice versa. The vertical variations of BGRC of the density of CEs and AEs are also very similar. The magnitude of the coefficients is very large near the surface and decreases rapidly with the depth, suggesting the variation of background SSH is mainly related to the upper oceanic dynamic process. For example, off West Australia, the upper LC with warm and fresh water intensifies in Austral fall and winter, then the dynamic adjustments make SSH rise (Table 1) and isopycnals depress (Feng et al., 2003), resulting in a negative density anomaly in the upper layer. The opposite case occurs in Austral spring and summer.

The eddy vertical structure can be inferred from the vertical variation of the EIRC of density. The depth with the maximal magnitude of EIRC of density (Figure 2b) is essentially the location of the eddy density core. The eddy density core of AEs is in the subsurface layer (~140 m), while CEs in the intermediate layer (~650 m). The maximal magnitude of EIRC of the density of AEs (-3.32 kg/m^4) is about twice that of CEs (-1.71 kg/m^4), indicating that if the amplitude of an AE is the same as that of a CE, the maximal density anomaly in the AE will be much stronger than that in the CE. Since the mean amplitude of AEs and CEs in the LC system are very close (Table 1), the maximal density anomaly in the average AE (-0.51 kg/m^3) is much stronger than that in the average CE (0.22 kg/m^3) (Figures 2c and 2d).

In the intermediate and deep layers, the magnitudes of density anomaly and EIRC of the density of AEs are much smaller than those of CEs (Figures 2b–2d). This is consistent with the correlation analysis (Figure 2a), indicating that AEs have little impact on the water motion in intermediate and deep layers. Furthermore, when comparing with the BGRC of density, the EIRC of density has a larger magnitude in the subsurface and deep layers (Figure 2a), indicating that the density anomaly in these layers is dominated by eddy rather than by background flow.

3.3. Temperature Anomalies in Eddies

Figure 3a shows the correlation between Argo observed and reconstructed temperature anomalies in CEs and AEs. The vertical profile of the correlation coefficients for temperature is similar to that for density (Figure 2a). Correlations in CEs and AEs are largest (over 0.7) from 460 to 920 m depth and 150–300 m depth, respectively. The correlation coefficient is positively correlated with the square of eddy-induced and background coefficients but inversely correlated with the variance of the error term (see Text S1). Here, depths with high correlations commonly have large eddy-induced temperature coefficients, except at depths below 900 m in CEs, where the eddy-induced temperature coefficient is below 5 °C/m but the correlation (from 0.55 to 0.7) is relatively high.

The EIRC of the temperature of CEs peaks at 600 m depth with a value of 15.42 °C/m, while that of AEs peaks at 260 m depth with a value of 13.43 °C/m, which indicates that CEs and AEs with an SLA of 10 cm are associated with variations in temperature anomalies of over 1.5 °C and 1.3 °C, respectively (Figure 3b). The EIRC of the temperature of CEs reverses its sign between 80 to 220 m depth as the EIRC of density (Figure 2b), indicating that the density anomalies in eddies are mainly related to the temperature anomalies. The background temperature coefficients of both CEs and AEs are largest (over 5 °C/m) at upper 380 m depth and relatively smaller at deep layer.

The average CE is characterized by large anomalies of up to −1.93 °C at 750 m depth. Anomalies colder than −1 °C extend from 250 to 800 m depth (Figure 3c). A secondary core with an anomaly of up to −1.52 °C is found at 330 m depth. A local minimum in the magnitude of the temperature anomaly occurs between those two cores (about 400–600 m), roughly coinciding with the depth of the Subantarctic mode water (SAMW) (Woo & Pattiaratchi, 2008). A local warm core is found at 130 m depth with a temperature anomaly of −0.18°C, where the eddy center is surrounded by relatively cold water. In the average AE, temperature anomalies in excess of 1 °C can be found from 50 to 400 m depth (Figure 3d). The temperature core of the

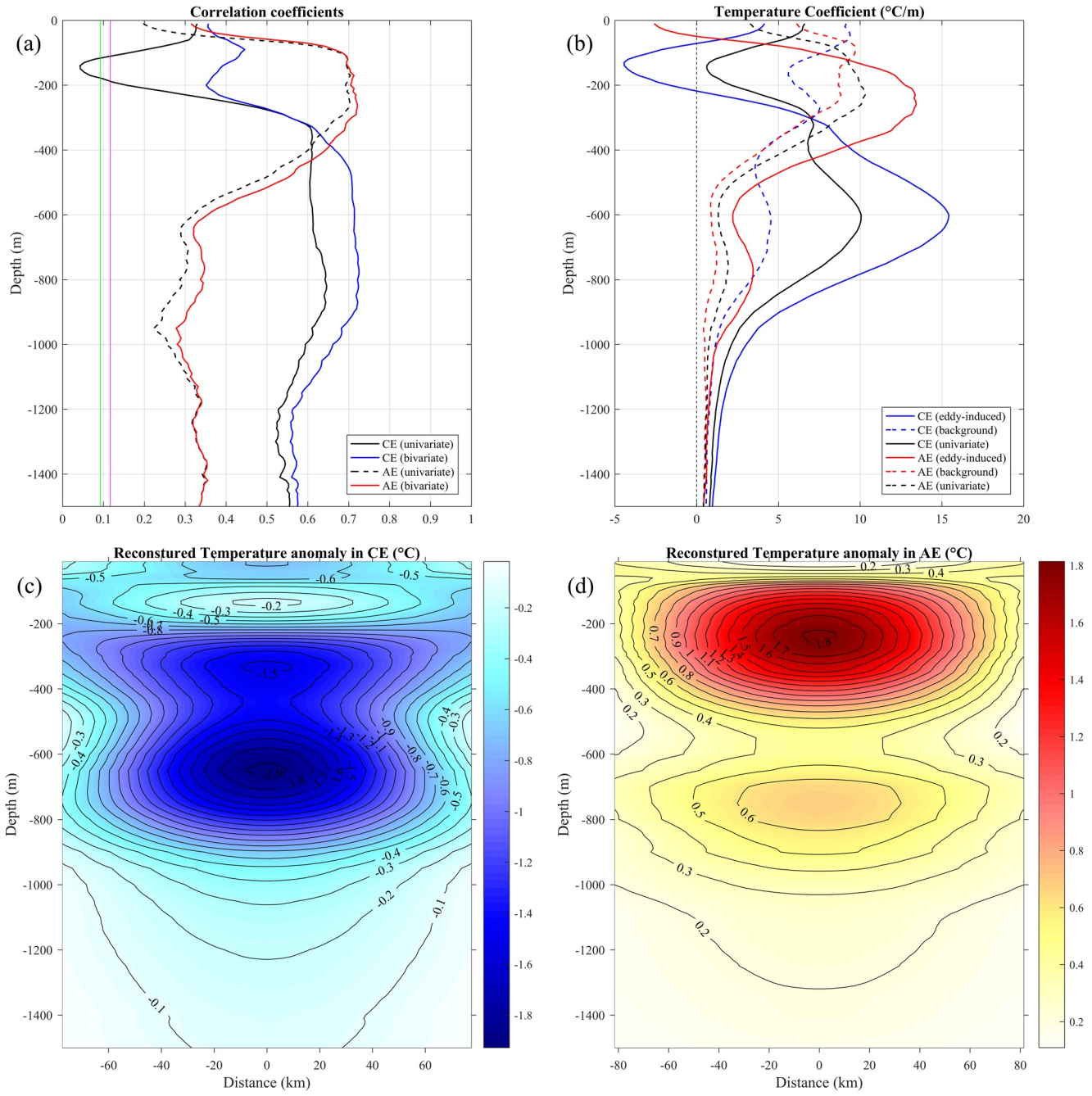

Figure 3. Same as Figure 2 but for the temperature.

average AE occurs at 230 m depth with a temperature anomaly of 1.81 °C, which is deeper than its density core. A secondary peak is in the intermediate water at 750 m depth with a temperature anomaly of 0.69 °C. Large temperature and density anomalies in eddies are commonly at depths with strong background stratification. In the LC system, the vertical density and temperature gradients of Subsurface Indian Center Water (SICW) in the subsurface layer and the Antarctic Intermediate Water (AAIW) in the intermediate layer are relatively larger than those in the SAMW, which is approximately at 400–600 m and characterized with low PV. Therefore, density and temperature anomalies in the average CE and AE are larger in the SICW and AAIW (Figures 2c, 2d, 3c, and 3d).

Usually, the water temperature in the center of CE is lower than that at the eddy edge, and vice versa in AE. This expects that the EIRC of temperature should be positive. The above analysis shows that it's true in most cases. An exception is at the subsurface (from about 100 to 200 m) in the average CE, where the temperature anomalies in the eddy center are warmer than those at the edge (Figure 3c). In this layer, the EIRC of temperature is negative, which is opposite to that at other depths (Figure 3b). This unusual phenomenon is also found in the EIRC of density and density anomaly in the average CE (Figure 2), which indicates that in the subsurface layer, the center of CEs usually contains a parcel of warm water, which may come from the eddy-trapped nearshore LC water and/or is due to the depression of the subsurface isotherm.

3.4. Salinity Anomalies in Eddies

The salinity coefficients for CEs and AEs (Figure 4b) are mostly negative with large magnitudes above 200 m depth, except for the eddy-induced coefficient in CEs, whose magnitude is relatively small. This indicates that the salinity anomalies above 200 m depth in a CE are not sensitive to its amplitude. From 200 to 800 m depth, all the salinity coefficients are positive with large magnitudes. At depths below 800 m, the magnitude of the eddy-induced salinity coefficients in CEs is significantly larger than the other coefficients, indicates that the salinity in deep water can be effectively affected by CEs with large amplitude.

Figure 4a shows the correlations between the Argo observed and reconstructed salinity anomalies in CEs and AEs. A distinctive feature of the correlations for the salinity compared to those for the density and temperature is that the correlations for the salinity in CEs (AEs) drop to a minimum at ~200 and ~800 (~900) m depth, where the profiles of the background and eddy induced salinity coefficients of CEs (AEs), respectively, cross the zero line (Figure 4b). Those depths correspond with the South Indian central water featured with salinity maximum and the AAIW featured with salinity minimum (Woo & Pattiaratchi, 2008). Therefore, the vertical gradient of salinity is approximately zero at those depths (see Figure S2), and the doming or depressing of the isohalines associated with the change of the SSH plays a minor role in the change of the local salinity.

The temperature variation of seawater is commonly the main factor for its density anomaly. However, the contribution of salinity variation could exceed that of temperature in deep water. Below 1,000 m depth, the correlations for the salinity in CEs, which range from 0.6 to 0.7 (Figure 4a), gradually exceed the correlations for the temperature (Figure 3a), indicating that the salinity anomalies could be reconstructed better than the temperature anomalies at deep water in CEs.

The average CE and AE are characterized by different layered structures in the salinity anomalies (Figures 4c and 4d), which are positive-negative-positive and negative-positive-negative from surface to 1,500 m depth, respectively. Those sandwich structures could be associated with the doming and depressing of isohalines in the CE and AE, respectively. Peak salinity anomalies are found at 330 m depth with a value of −0.21 psu for the average CE and at 320m depth with a value of 0.25 psu for the average AE. At the top 200 m of the water column, the magnitude of salinity anomalies is larger for the AE, which has a local minimum at 90 m depth with a value of −0.21 psu. This may be caused by the joint effect of the vertical isohaline displacement in AEs and the trapped low salinity water from the LC.

3.5. Geostrophic Velocities in Eddies

According to Equations 24 and 25, the vertical mode $H(z)$ is the ratio of geostrophic velocity at depth z to that at the surface. Both the vertical modes of the CEs and AEs are close to 1 at 10 m depth (Figure 5a), indicating that it is reasonable to set 1,500 m as the level of no motion. However, these modes have very different vertical profiles. The maximum of the vertical mode of CEs is in the subsurface layer (240 m), which is one of the main features of the subsurface-intensified eddy. Below 240 m, this mode decreases slowly. At 740 m, the average CE still has approximately half the magnitude of the surface velocity (Figure 5c). The vertical mode of the AEs is surface-intensified and decreases steeply with increasing depth in the upper 300 m (Figure 5a). Therefore, the reconstructed geostrophic velocity in AEs has a strong baroclinic structure in the upper layer, which is consistent with previous observations (see Figure S3).

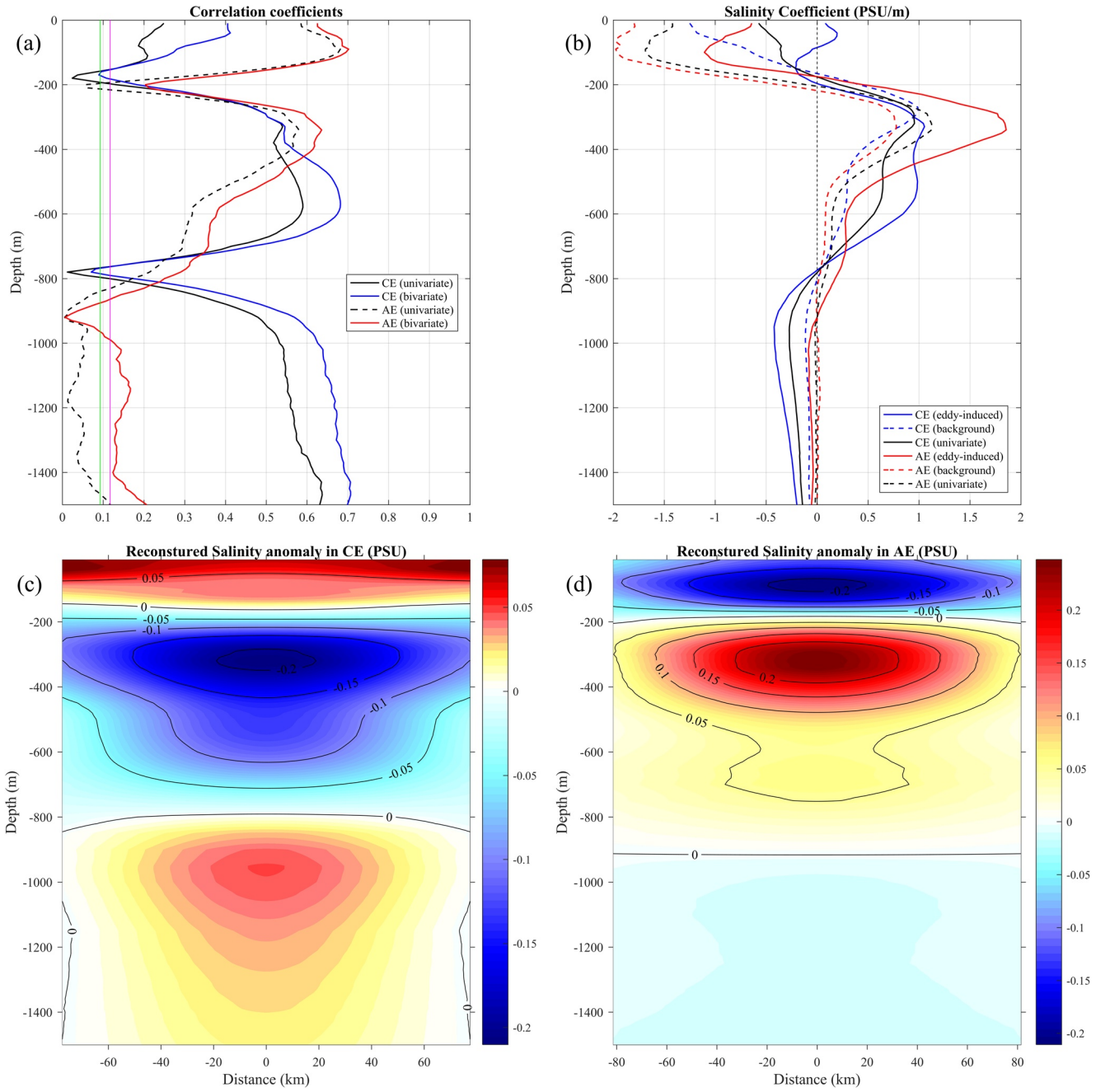

Figure 4. Same as Figure 2 but for the salinity.

The vertical mode of the CEs shows an S-shaped structure above 400 m depth; specifically, with increasing depth, it decreases gradually from the surface of 0.98, reaches a local minimum of 0.94 at 70 m, and then increases gradually until 240 m, where it peaks at a value of 1.04. This profile is identical to the in-situ observation of a CE in Feng et al. (2007) (see Figure S3). In addition, the S-shaped structure is also seen in subsurface-intensified eddies in other oceans (e.g., Chaigneau et al., 2011). The increase of the vertical mode in the subsurface layer coincides with the negative density anomaly in the CEs, which may be caused by the depression of isopycnal or trapped warm water from the LC. From a T-S diagram of eddy center water (see Figure S4), the average AE contains LC water in the upper 200 m, which is characterized by high temperature and low salinity.

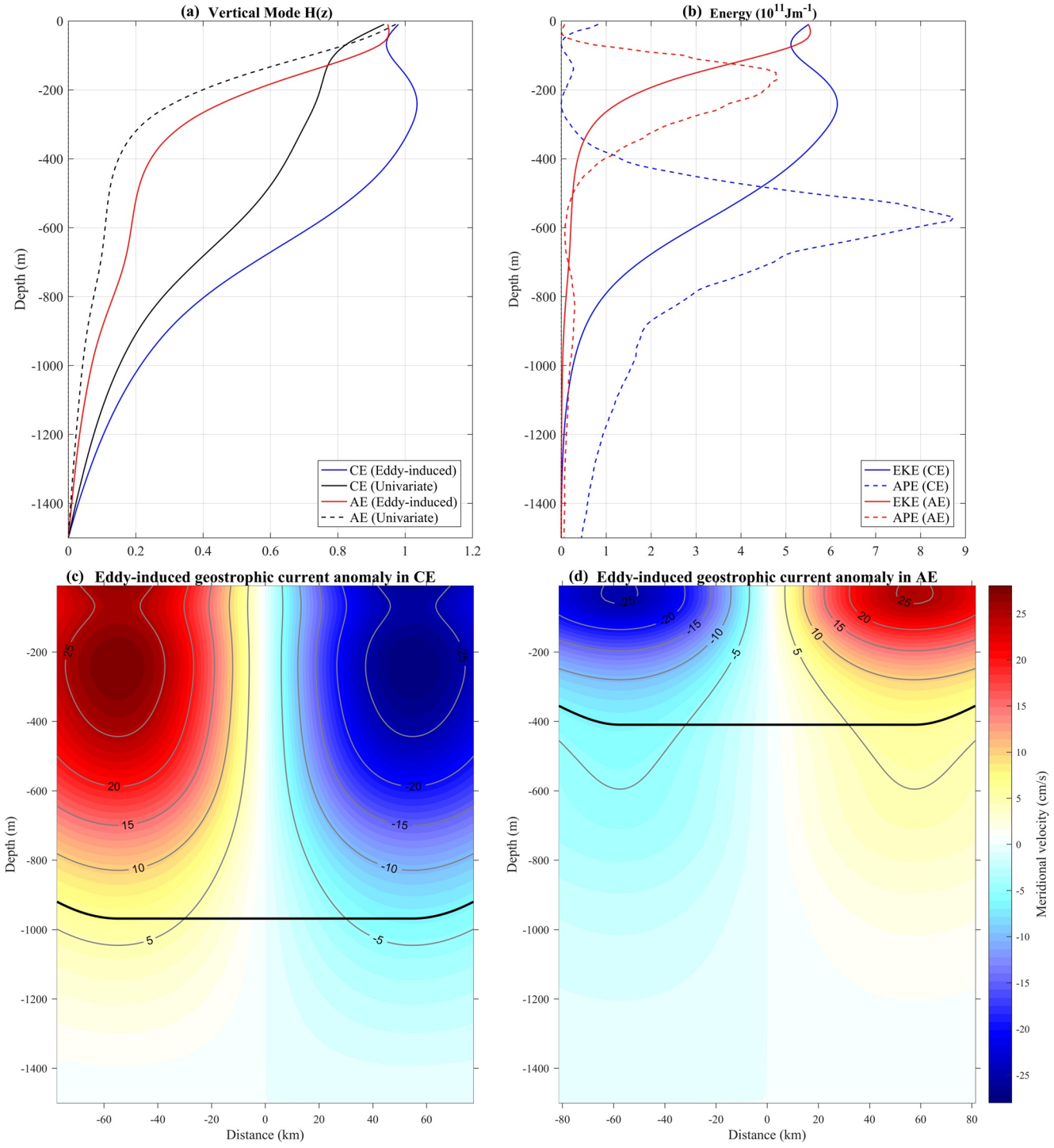

Figure 5. Eddy vertical mode, area integrated energy, and geostrophic velocity anomaly of the average CE and AE as a function of depth. (a) Blue (red) line denotes eddy-induced vertical mode $H(z)$ of CEs (AEs). Solid (dashed) black line denotes the vertical mode of CEs and AEs which is not distinguished the background and eddy-induced effects. (b) Solid (dashed) blue and red lines denote the area integrated EKE (APE) of the average CE and AE, respectively. Black lines in (c) and (d) denote the trapping boundary of the average CE and AE, respectively. AE, anticyclonic eddies; CE, cyclonic eddies.

3.6. Eddy Energy

Equation 28 shows that the area-integrated EKE is proportional to the square of the eddy amplitude A^2 and vertical mode H^2. Therefore, the vertical profile of the area-integrated EKE (Figure 5b) is analogous to that of the vertical mode (Figure 5a). The volume-integrated EKE, which is calculated by the depth integration of $K(z)$ from the surface to 1,500 m, depends on the eddy amplitude A and the depth integral of the square of vertical mode H^2. Given that the mean amplitudes of AEs and CEs are similar (Table 1), the difference of volume-integrated EKE between average AE and CE mainly depends on the depth integral of the square of vertical mode. Since AEs are strongly baroclinic in the upper layer, the vertical mode of AEs decreases more rapidly with depth than that of CEs (Figure 5a). As a result, the depth integral of the square of the vertical mode of CEs will be much larger than that of AEs. Here, the volume-integrated EKE of the average CE (3.57×10^{14} J) is 3.4 times that of the average AE (1.06×10^{14} J).

Equation 29 shows that the area-integrated APE is proportional to the square of the eddy radius R^2, amplitude A^2, and the ratio between EIRC of density and buoyancy frequency $\left(\frac{\alpha_\rho}{N}\right)^2$. The depth of maximal area-integrated APE (Figure 5b) is basically the same as that of the EIRC of density α (Figure 2b), that is, the eddy density core usually has the maximal APE. Although the maximal EIRC of the density of AEs is significantly larger than that of CEs, the buoyancy frequency in the intermediate layer is much smaller than that in the subsurface layer, so the area-integrated APE in the core of the average CE is approximately twice that in the average AE. Moreover, the volume-integrated APE of the average CE (3.00×10^{14} J) is significantly larger than that of the average AE (1.22×10^{14} J).

Previous studies have shown that the lifespan of eddies is positively correlated with their amplitude or radius (Chaigneau et al., 2008; Chen et al., 2011). A common feature is that these two eddy properties can affect the total EKE and/or APE of eddies. Since the life cycle of eddies is essentially a process of the conversion and dissipation of mesoscale energy, the lifespan of eddies could be directly related to their energies. The above results of eddy energy show that, on average, CEs in the LC system have larger EKE and APE than AEs, which could lead to a longer lifespan of CEs.

3.7. Eddy-Induced Volume Transport

Previous studies show that eddies can transport coastal water offshore to impact the water mass and ecosystem in the ocean interior (Fieux et al., 2005; Moore et al., 2007). In this section, we will estimate the eddy-induced volume transport in the LC system. Nonlinear eddies can transport water, heat, and salt above their trapping depths (Castelao, 2014; Chelton et al., 2011; Flierl, 1981). The eddy-induced volume transport at a point p inside an eddy e_1 is estimated as:

$$V_{\text{eddy}}(z) = \begin{cases} \overrightarrow{u_d}, p \in \Gamma_{\text{trap}}(z) \\ 0, \quad p \notin \Gamma_{\text{trap}}(z) \end{cases} \tag{30}$$

where $\overrightarrow{u_d}$ is the drift velocity of eddy e_1 and $\Gamma_{\text{trap}}(z)$ is the trapping boundary of the eddy e_1 at depth z (see Text S2 for detail). Figures 5c and 5d denote the trapping boundary in the average CE and AE, respectively.

Unlike the eddy-induced transports estimated by previous studies (e.g., Castelao, 2014; Chaigneau et al., 2011), which are mostly based on the average three-dimensional structure and eddy propagation velocity, we calculated the eddy-induced transports at each grid point on every day, and then obtained the average three-dimensional structure of eddy-induced transports by time averaging. In addition, we use the instantaneous eddy propagation velocity to estimate the trapping depth and eddy-induced transports rather than the average eddy propagation velocity. The latter one may overestimate the eddy volume transport by 25% (Figure S5).

The volume transport by eddy movement is mostly westward (Figures 6a and 6b, 6c). The volume transport by CEs is about two times that by AEs, with a magnitude of approximately 6 and 3 m^2/s in offshore areas, respectively. The volume transport by all eddies (Figure 6c) is within the same order of magnitude as the transport by annual-mean circulation from Furue et al. (2017) (Their study was restricted to the upper

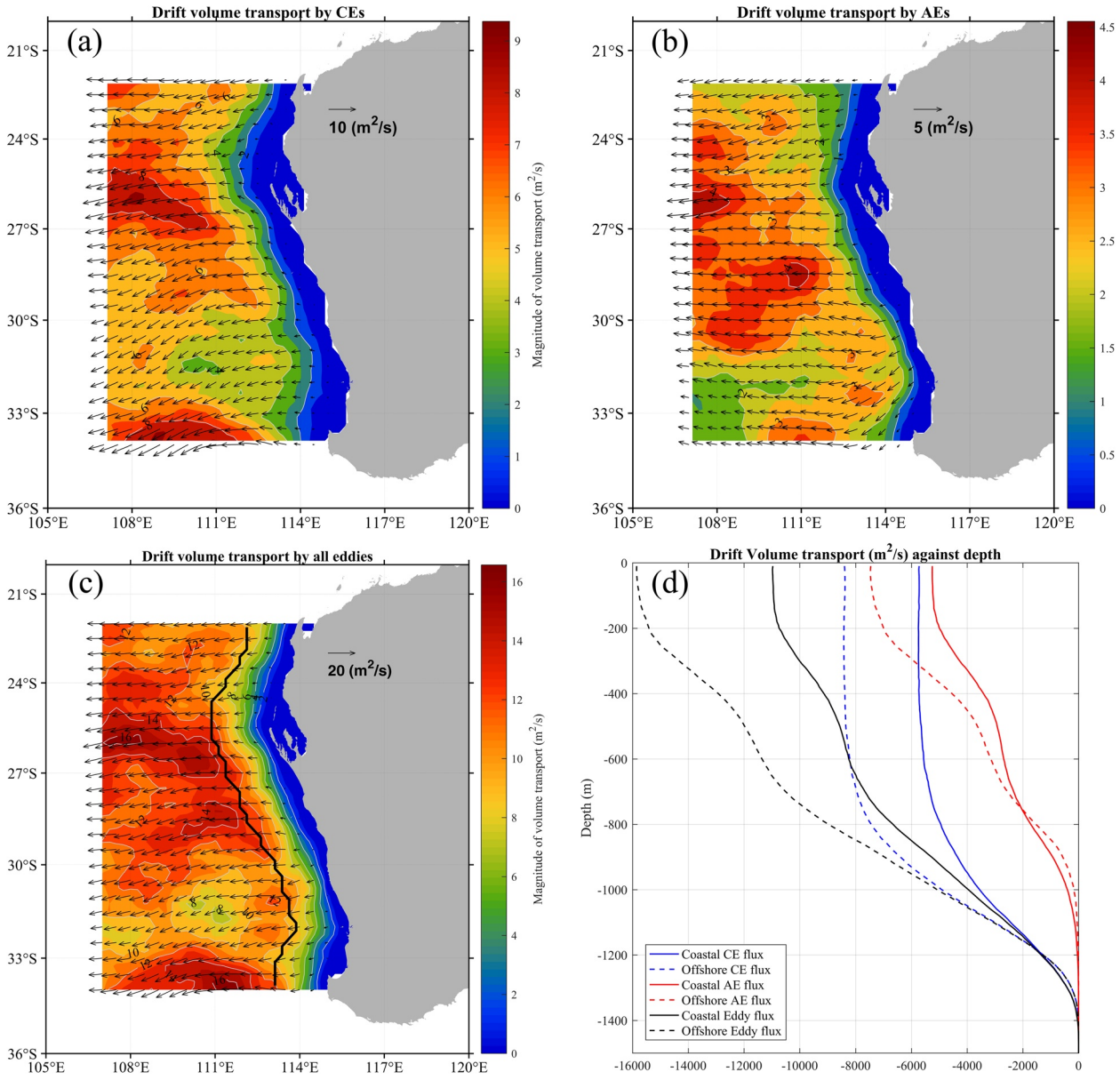

Figure 6. Eddy-induced volume transport (m^2/s, vectors) and its magnitude (m^2/s, color shading) by (a) CEs, (b) AEs, (c) all eddies, and (d) volume transports with depth across the coastal (solid lines) and offshore (dashed lines) sections by CEs (blue lines), AEs (red lines) and all eddies (black lines). AE, anticyclonic eddies; CE, cyclonic eddies.

900 m, where the LC and LUC dominate). From surface to 200 m, the annual-mean eddy volume transport across the coastal section is 2.2 Sv; From 200 to 900 m, this transport is 5.8 Sv, which is higher than the offshore transport by the mean circulation (3.6 Sv from 28°S to 22°S) (Furue et al., 2017).

The above results show that the zonal volume transport by eddies is even larger than that by the mean flow under 200 m. It should be noted that the compensated flow of the eddy volume transport is different from that of the mean flow. The compensated flow of the subsurface westward flow is from the LUC and the downwelling of the LC (Furue, 2019; Furue et al., 2017). However, the compensated flow of the volume transport by an eddy may be mainly from the water around this eddy. For example, when the AE simulated by Early et al. (2011) propagates westward, a part of the background water slightly migrates eastward compensating the eddy volume transport (see Figure 13 in Early et al. 2011). Therefore, the eddy volume trans-

port could effectively promote the water exchange between the coastal and offshore water and contribute to the westward spread of the SAMW and AAIW.

3.8. Eddy-Induced Heat and Salt Transports

3.8.1. Estimating Eddy-Induced Heat and Salt Transport

The composite eddy-induced SSTA (Figure 7) was constructed by rotating the coordinate system for each eddy realization to align the background SST gradient to equatorward and normalizing by the eddy radius (see Text S3 for detailed method). The extremum of SSTA in composite CE (Figure 7a) is in the northwest quadrant with a value below −0.4 °C, while the extremum of SSTA in composite AE (Figure 7b) is in the southwest quadrant with a value over 0.5 °C. The composite eddy-induced SSTA can be interpreted as a superposition of an axisymmetric monopole core of cold (warm) water and a dipole SSTA structure (Gaube et al., 2015). Here the SSTA monopole is assumed to be axisymmetric and calculated by the radial average of the composite eddy-induced SSTA. Then the residuals are the SSTA dipole. The monopole core (Figures 7c and 7d) is associated with the upwelling (downwelling) centered on the eddy interior or water trapped in the eddy interior, while the dipole structure (Figures 7e and 7f) is caused by eddy-driven horizontal advection of the isotherm.

Two mechanisms are associated with horizontal eddy heat/salt transport (Czeschel et al., 2018): (1) eddy transport of water masses trapped in the eddy interior, also called "drift heat/salt transport" (Hausmann & Czaja, 2012) and (2) eddy stirring, which occurs at the periphery of the eddy, also called "swirl heat/salt transport" (Hausmann & Czaja, 2012). The "drift heat/salt transport" is associated with the monopole structure of the temperature/salinity anomaly in the eddy, while the "swirl heat transport" is associated with the dipole structure of the temperature/salinity anomaly in the eddy.

Previous studies on the eddy vertical structure show that the eddy-induced temperature anomaly is non-axisymmetric at the surface (e.g., Hausmann & Czaja, 2012), and quickly change to axisymmetric structure with increasing depth (e.g., Cheng et al., 2018; He et al., 2018; Yang et al., 2015). The swirl heat transport peaks in the mixed layer, and decreases rapidly with depth. Therefore, although the mixed layer depth (MLD) only accounts for a small portion of the "eddy trapped depth," it contained a considerable proportion of the total eddy swirl heat transport.

Since we have not reconstructed the dipole structure in the subsurface layers of the eddy, we only estimate the swirl heat transport in the mixed layer following Hausmann and Czaja (2012):

$$H_{\text{swirl}} = \rho_0 C_p \overrightarrow{u_g} h_{\text{ml}} \text{SST'}, \tag{31}$$

where $\overrightarrow{u_g}$ is the high-pass filtered (270 days) geostrophic current velocity derived from satellite SLA data, h_{ml} is the monthly MLD climatology from CSIRO Atlas of Regional Seas 2009 (CARS09) (Condie & Dunn, 2006), and SST' is the high-pass filtered (270 days) satellite observed SSTA.

The drift heat transport at a point p inside an eddy e_1 is estimated as:

$$H_{\text{drift}}(z) = \begin{cases} \rho_0 C_p \overrightarrow{u_g} \widehat{T'}, p \in \ _{\text{trap}}(z) \\ 0, \quad p \notin \ _{\text{trap}}(z) \end{cases} \tag{32}$$

where $\rho_0 = 1025\ \text{kg m}^{-3}$ is the mean sea water density, $C_p = 3989\ \text{Jkg}^{-1}.^{\circ}\text{C}^{-1}$ is the specific heat capacity of sea water, and $\widehat{T'}$ is the reconstructed eddy temperature anomaly.

Similarly, the drift salt transport at a point p inside an eddy e_1 is estimated as:

$$S_{\text{drift}} = \begin{cases} \rho_0 \overrightarrow{u_g} \widehat{S'}, p \in \ _{\text{trap}}(z) \\ 0, \quad p \notin \ _{\text{trap}}(z) \end{cases} \tag{33}$$

where $\widehat{S'}$ is the reconstructed eddy salinity anomaly.

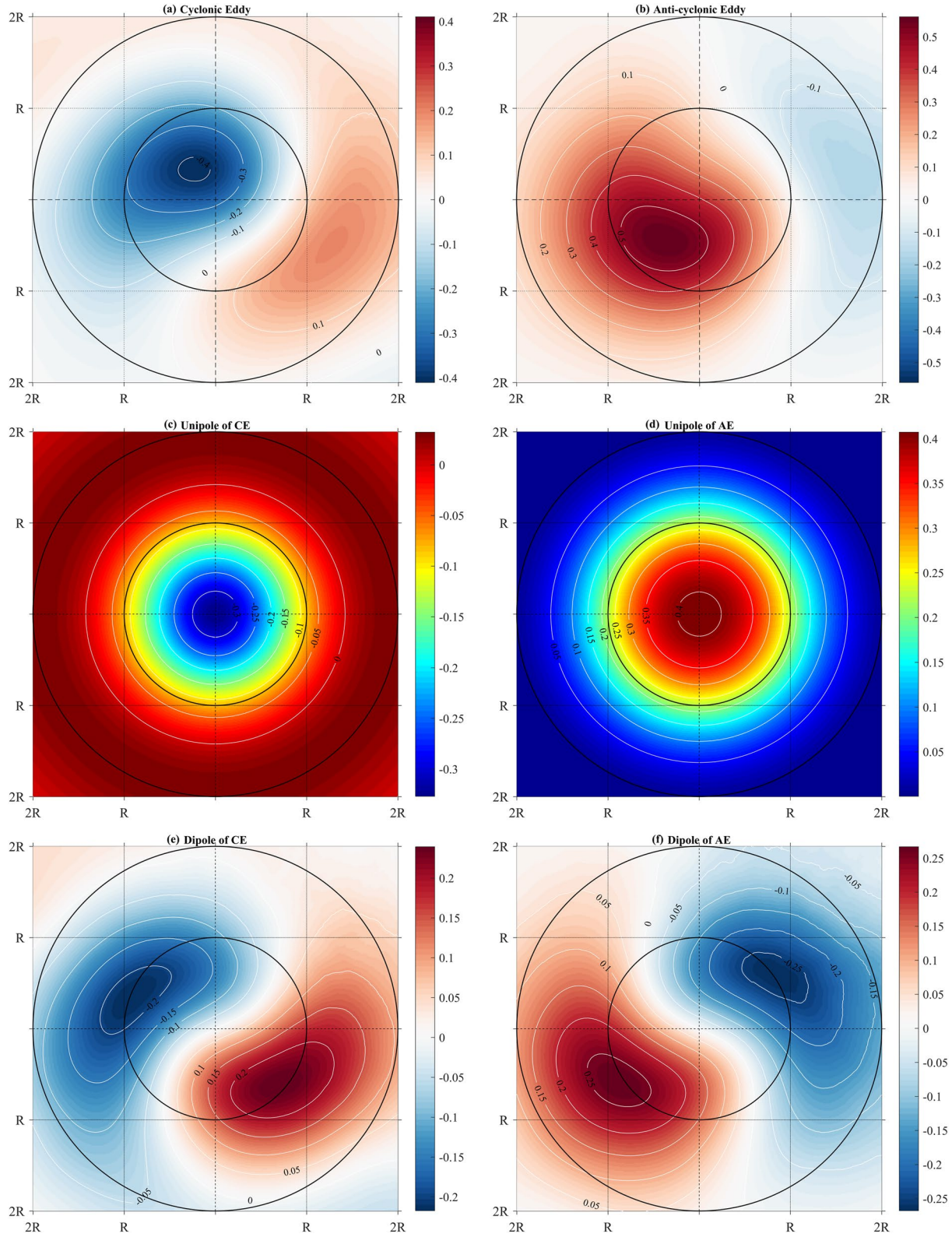

Figure 7. Composite SSTA (°C, contours and color shading) in (a) CEs, (b) AEs and (c), (d) their monopole and (e), (f) dipole structures. The composite averages were constructed by rotating the coordinate system for each eddy realization to align the background climatology SST gradient to a polar angle of 90°. AE, anticyclonic eddies; CE, cyclonic eddies; SSTA, sea surface temperature anomaly.

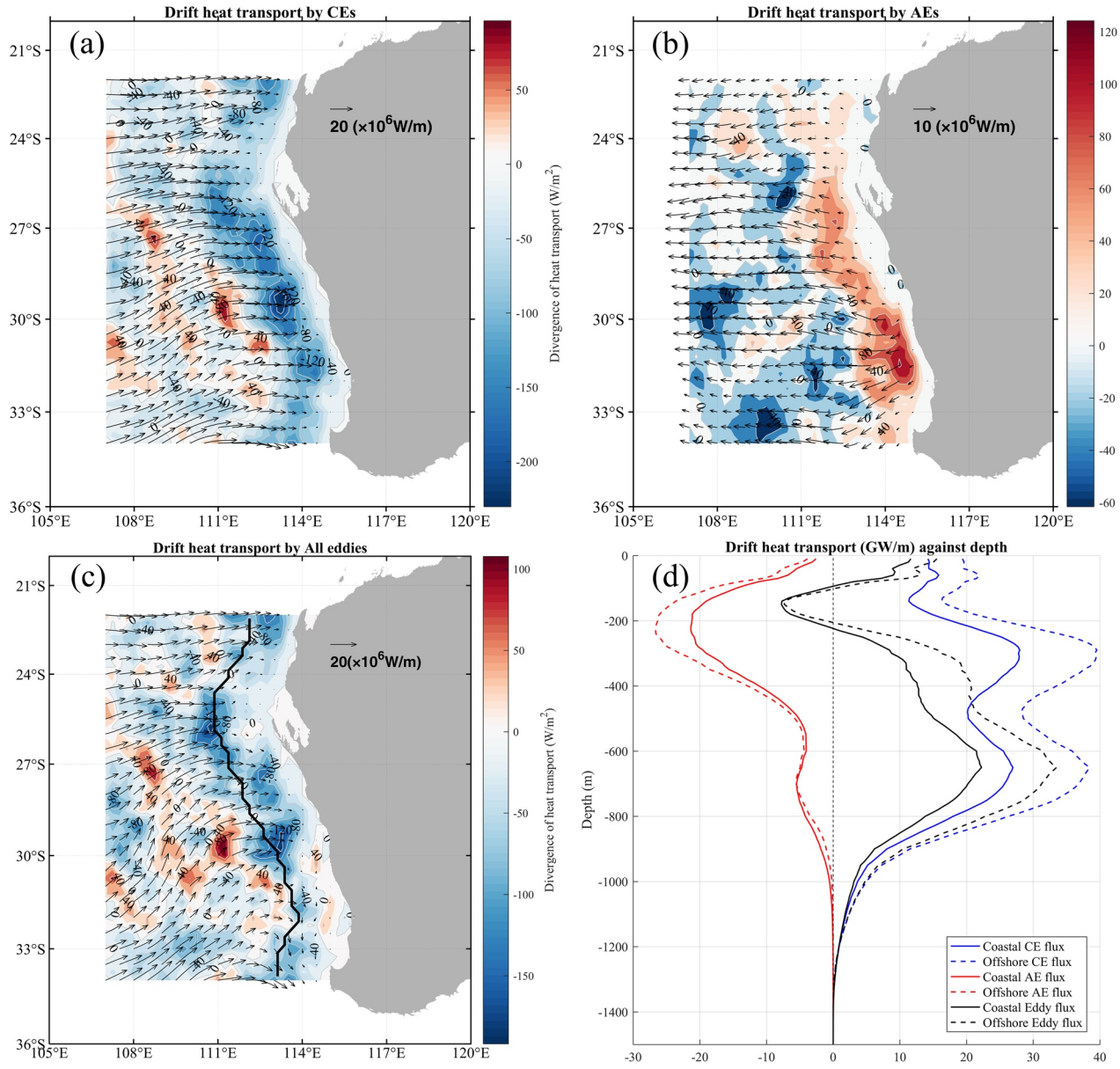

Figure 8. Same as Figure 6 but for eddy drift heat transport (10^6 W/m, vectors) and its divergence (W/m^2, color shading).

3.8.2. Eddy Drift Heat Transport

Figure 8 shows the spatial distribution of time-average eddy drifts heat transport from 1993 to 2016. CEs trapped cold water propagate offshore, which is equivalent to transport heat from offshore to nearshore. The magnitude of drift heat transport by CEs (Figure 8a) is approximately 15–25 MW/m and mostly transport eastward or northeastward, leading to warm up the nearshore area, where the convergence of heat is up to more than 160 W/m^2 at about 113°E, 29.5°S. On the contrary, AEs transport heat from nearshore to offshore (Figure 8b). The magnitude of drift heat transport by AEs is approximately 6–12 MW/m, which is far less than CEs. AEs tend to cool down the nearshore area, where the divergence of heat is up to 120 W/m^2 at about 114.5°E, 31.5°S.

The pattern of drift heat transport by all eddies (Figure 8c) resembles to that of CEs, which have a characteristic magnitude of 12–20 MW/m and mostly eastward or northeastward. The summation of all eddies' effects is warming up the nearshore area, whose convergence is up to 120 W/m^2. A remarkable feature of

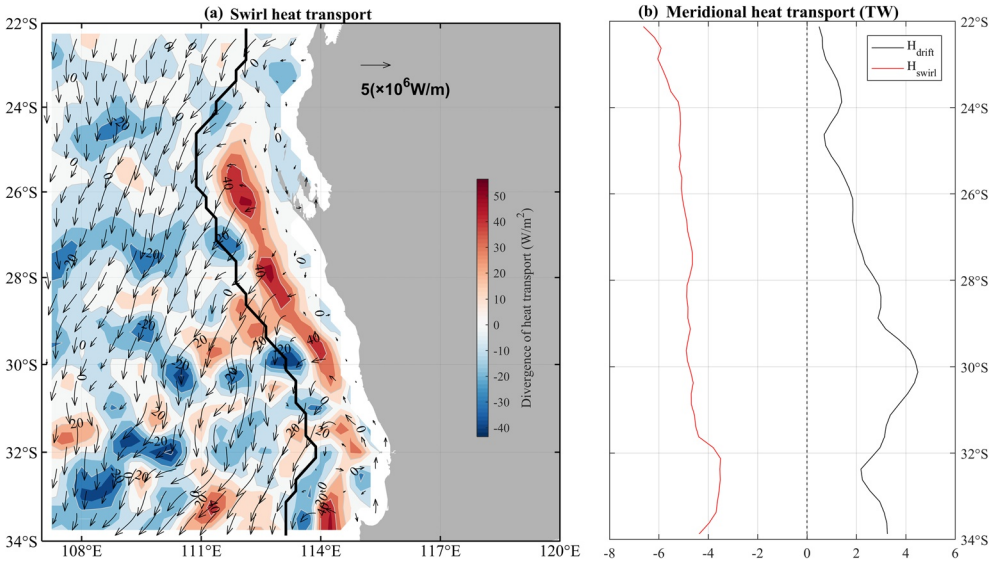

Figure 9. (a) Eddy swirl heat transport (10^6 W/m, vectors) and its divergence (W/m^2, color shading) and (b) the meridional heat transport integrated from 107°E to the coast by eddy drift (black line) and eddy swirl (red line).

Figure 8c is that the meridional heat transport has a prominent equatorward component in the south of 27°S, where the zonal integrated meridional heat flux from 107°E to the coastline is over 2 TW (Figure 9b). This is consistent with the poleward displacement of CEs in this region (Morrow et al., 2004).

Figure 8d shows the vertical structure of eddy drift heat transport across the coastal and offshore sections. The coastal section, which is 1.5° off the 200 m isobaths, separates the LC system from the ocean interior. The offshore section is at 107°E, which is the western boundary of the study region. AEs transport heat westward in all depths and have large transport (>10 GW/m) from 100 to 400 m depth. In contrast, CEs' heat transport is eastward in all depths. They peak at approximately 200 and 680 m depth with a value over 25 GW/m.

The drift heat transport of all eddies across the coastal section (Figure 8d) is westward between 100 and 200 m, where AEs dominate over CEs in this depth range. The maximum westward transport is at about 150 m with a value of 8 GW/m. However, at the other depths, the transport is eastward and dominated by CEs. The maximal eastward transport is at about 650 m with a value of 22 GW/m. The vertical variations of transport across the offshore section are similar to that across the coastal section but with a larger magnitude.

3.8.3. Eddy Swirl Heat Transport

The eddy swirl generally transports heat poleward and offshore with a magnitude of approximately 4 MW/m (Figure 9a), which is opposing the time-averaged SST gradient. On the zonal integration (117°N to the coastline), the meridional heat transport by eddy swirl is poleward with a magnitude of approximately 5 TW, while is significantly larger than that by eddy drift (Figure 9b). The eddy stirring tends to cool down the LC catchment, which is in agreement with the previous model study (Domingues et al., 2006). The divergence of eddy swirl heat flux is up to over 50 W/m^2.

The mean swirl heat transport across the coastal section is −2.33 TW (eastward positive), whose magnitude is significantly smaller than that of the drift heat transport (10.66 TW). However, the swirl heat transport is mainly concentrated on the shallow mixed layer. Given that the average MLD of the coastal section is 41.65 m, the average swirl heat transport per meter depth is −55.94 GW/m, whose magnitude is much larger than that of the drift heat transport (approximately 10 GW/m, Figure 8d).

The mean swirl heat transport across the offshore section is −0.60 TW, which is much smaller than that of the drift heat transport (17.12 TW). The averaged MLD of this section is 50.53 m and the depth-averaged swirl heat transport in the mixed layer is −11.85 GW/m, which is comparable with that of the drift heat

transport. Although we did not calculate the swirl heat transport below the mixed layer, according to the feature of rapid decrease with a depth of the swirl heat transport (He et al., 2018), the eddy heat transport below the subsurface should be dominated by the drift transport.

Combining with the eddy swirl and drift heat transport, the heat is transported offshore by eddies above 200 m depth, cooling down the LC, while eddy heat transport is onshore below 200 m depth, warming up the LUC. The convergence/divergence of eddy-induced heat transport is about −120 to 80 W/m^2, which is comparable with the surface air-sea heat flux with the value of −200 to 100 W/m^2 (Feng et al., 2003), indicating eddies play an important role on the heat balance of the southeastern Indian Ocean.

3.8.4. Eddy Drift Salt Transport

The spatial pattern of time-averaged eddy drift salt transport (Figures 10a–10c) is similar to that of eddy drift heat transport, which is characterized by the onshore transport by CEs and offshore transport by AEs. The magnitude of drift salt transport by CEs is approximately 0.25 kg/ms, while that by AEs is approximately 0.1 kg/ms. Therefore, the drift transport by all eddies is onshore with a magnitude of approximately 0.2 kg/ms. The convergence of drift salt transport by CEs is up to more than 2×10^{-3} g/m^{2}s at around 113°E, 28°S and 113.5°E, 29.5°S, while the divergence of drift salt transport by AEs is up to more than 2×10^{-3} g/m^{2}s at around 114.5°E, 31°S. On the meridional direction, the drift salt transport by all eddies has a prominent equatorward component south of 27°S, which is similar to the eddy drift heat transport.

The divergence/convergence of the eddy drift salt transport is in order of 10^{-3} g/m^{2}s (Figure 10c), which is equivalent to a fresh water flux of 2.4 mm/day. This value is close to the surface freshwater flux with a value of approximately 3 mm/day (Feng et al., 2003), indicating that the eddy salt transport could play an important role in the salinity variability in the southeastern Indian Ocean.

The vertical structures of drift salt transport by CEs and AEs across the coastal section (Figure 10d) are consistent with the salinity anomalies in the average CE and AE, respectively. In depths shallower than 200m, the drift salt transport by AEs across the coastal section is eastward, suggesting AEs transport fresh water of the LC offshore. Below 200 m depth, the direction of drift salt transport by AEs across the coastal section is westward. The vertical structure of drift salt transport by CEs has a sandwich structure, which is positive at 160–800 m and negative at other depths. The drift salt transport by all eddies across the coastal section is eastward from 50 to 750 m with a magnitude of approximately 300 kg/ms and westward in other depths with a much smaller magnitude, suggesting that eddy salt transport can make the downstream of the LC and LUC salty. The vertical structure of eddy drift salt transport across the offshore section is similar to that across the coastal section, but with a larger magnitude.

4. Summary and Discussion

Satellite observed SSHs were combined with decade-long in situ measurements of Argo floats to study the vertical structure of mesoscale eddies in the LC system. Based on an eddy tracking scheme and available Argo profiles, we devised a new eddy construction method. We considered the different effects of background and eddy-induced SSHAs on the eddy density, temperature, and salinity anomalies, and expressed these anomalies as linear functions of two types of SSHAs. Based on the obtained reconstruction coefficients and eddy statistics, we studied the vertical structures and energetics of eddies and estimated the eddy-induced volume, heat, and salinity transports.

We found that, averagely, the lifespan of CEs is significantly longer than that of AEs in the LC system, but there is almost no difference in amplitude and radius between CEs and AEs. Further analyses reveal distinct vertical structures between CEs and AEs. AEs in this region are usually surface-intensified, which weaken significantly below 500 m. The geostrophic current in the AEs peaks near the surface and decreases sharply with increasing depth. The cores of the density and temperature anomalies of the average AE are, respectively, at 130 m with a density anomaly of −0.51 kg/m^3 and 230 m with a temperature anomaly of 1.81 °C. In contrast, CEs are usually subsurface-intensified and extend to depths over 1,500 m. The geostrophic current in the CEs peaks at 240 m and shows an S-shaped vertical structure above 400 m depth. The cores of the density and temperature anomalies of the average CE are, respectively, at 650 m with a density anomaly of 0.24 kg/m^3 and 750 m with a temperature anomaly of 1.93 °C. The volume-integrated EKE and APE of

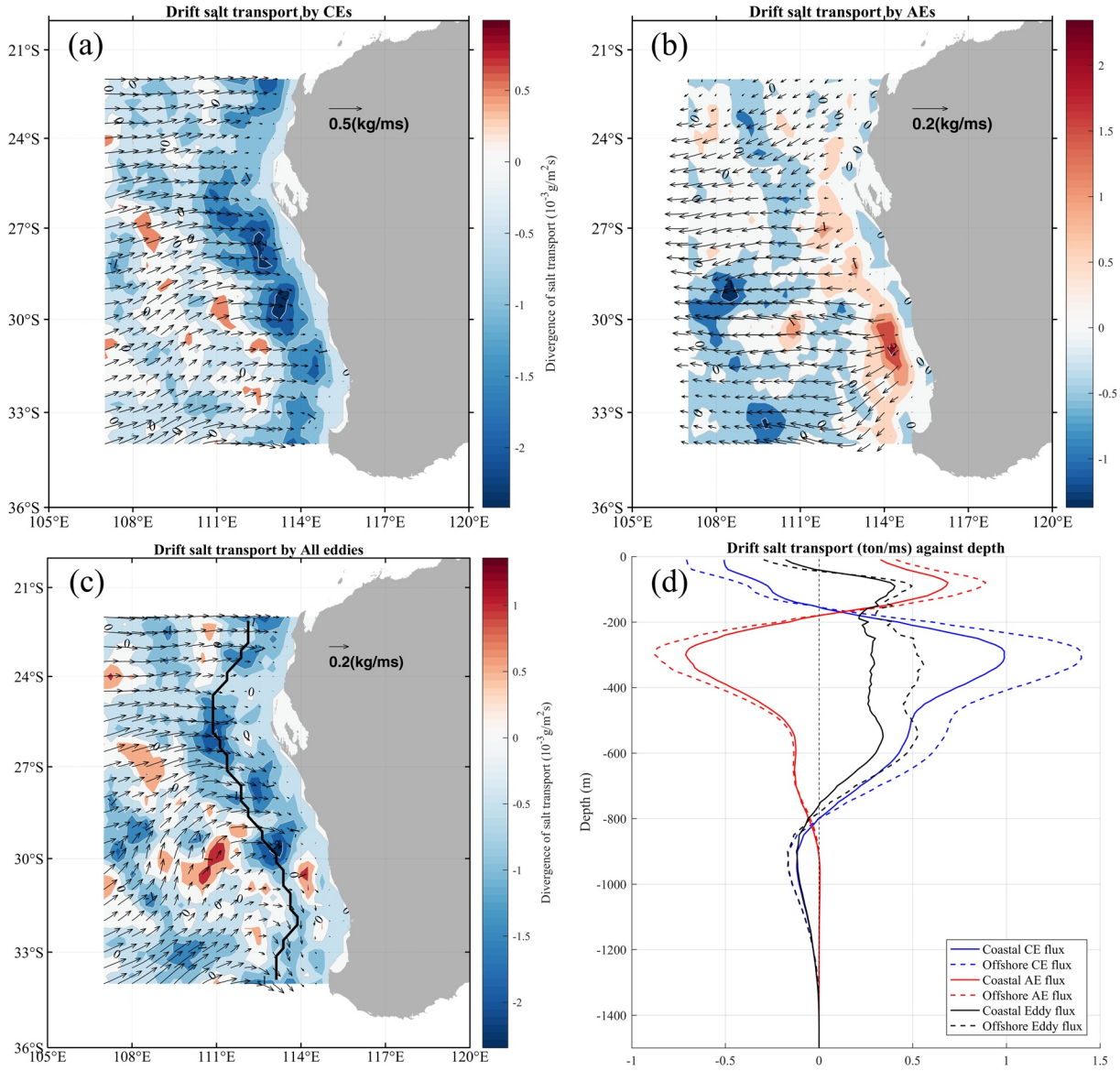

Figure 10. Same as Figure 6 but for eddy drift salt transport (kg/ms, vectors) and its divergence (10^{-3} g/m^{2}s, color shading).

the average CE are much larger than those of the average AE. The energy difference between CEs and AEs could contribute to their different lifespan.

There are distinct vertical structures between the CEs and AEs in other eastern boundary systems (Pegliasco et al., 2015). In the Peru-Chile Current System, the CEs are commonly surface-intensified with their cores at ~150 m, while the AEs are commonly subsurface-intensified with their cores at ~400 m (Chaigneau et al., 2011). Similarly, in the California Current System, the CEs are commonly surface-intensified with their cores at ~125 m, and some AEs are subsurface-intensified with their cores at ~400 m (Kurian et al., 2011; Pegliasco et al., 2015). In contrast, this study shows that CEs in the LC system is commonly subsurface-intensified and AEs are surface-intensified. A common feature in the above eastern boundary systems is that the density core of the CEs is usually at the depth of the equatorward current, while that of the AEs is at the depth of the poleward current.

When an ocean current flows southward, it gains positive vorticity due to the conservation of the PV, which is in favor of the generation of AEs in the Southern Hemisphere. On the contrary, a northward ocean cur-

rent will gain negative vorticity, which in favor of the generation of CEs in the Southern Hemisphere. Using a numerical simulation, Rennie et al. (2007) found that the generation of eddies in the LC system could be categorized into two types: (1) formed in the LC as a warm-core AE with a maximum velocity at the surface, which decreased rapidly with depth and (2) formed in the LUC, had a maximum velocity and coherent structure at 400–600m but became weaker toward the surface. This explains why the vertical structures of CEs and AEs are significantly different. Meanwhile, our study is consistent with the vertical structure simulated by Rennie et al. (2007).

Gaube et al. (2015) suggest that the decay time of an eddy is proportional to the vertical scale of the eddy and inversely proportional to the wind speed. The vertical scale of an eddy, D, can be estimated as:

$$D = \int_{-h}^{0} H(z)dz, \tag{34}$$

where h is the trapping depth of the eddy. The trapping depth of the average CE and AE are estimated as 1,041 and 562 m, respectively, where the nonlinear parameter equal to 1. In addition, the vertical mode $H(z)$ of CEs is larger than that of AEs in all depths (Figure 5a). The vertical scale of CEs (745 m) is significantly larger than that of AEs (268 m), which could explain why CEs have a longer lifespan than AEs in this region. Note that the lifespan difference between CEs and AEs in the LC system is opposite to that in the global oceans, where Chelton et al. (2011)'s global eddy census shows a preference for the eddies with a long lifespan to be anticyclonic. In global oceans, there are far more observation reports of subsurface-intensified AEs (e.g., Barceló-Llull et al., 2017; Hormazabal et al., 2013; Steinberg et al., 2019; Z. Zhang et al., 2015) than those of subsurface-intensified CEs. This could be one of the reasons why there are more long-lived AEs than long-lived CEs in global oceans.

We compared the reconstruction result, which does not consider the impact of the background flow. Castelao (2014) noted that the eddy SSHA is significantly correlated with its temperature and salinity anomalies. Thus, a linear regression of the form

$$\Theta'(z) = a(z) \cdot \eta' + b(z), \tag{35}$$

where Θ' is either density, temperature, or salinity anomalies, can be used to reconstruct tracer Θ. In this result, the density and temperature coefficients of the CEs do not reverse their signs at the subsurface (Figures 2 and 3b); thus, the vertical mode does not have an S-shaped structure but shows a surface-intensified structure (Figure 5a). The correlation of the predicted density or temperature with the observed one in CEs is also extremely low at the subsurface (Figures 2a and 3a), especially at ~200 m, and the correlation coefficient is only ~0.1. When the background SSHA is considered, the reconstructed density and temperature of the CEs are significantly improved from the surface to 250 m (Figures 2a and 3a). This suggests that the background flow plays a more important role than CEs at those depths. In addition, the result for CEs is also improved below 400 m (Figures 2a, 3a, and 4a), where the correlations can be increased by 0.05–0.1. However, the correlations for the AEs (Figures 2, 3b, and 4b) are only slightly improved when considering the background SSHA. It may be because the background and eddy-induced coefficients do not differ substantially at most depths.

According to previous observation and numerical simulations of eddies, the following features of eddies should be considered for a better eddy reconstruction result in the future. First, there may be several types of CEs or AEs with different vertical modes in this region. Dilmahamod et al. (2018) reported that there are some surface-intensified CEs and subsurface-intensified AEs in the South Indian Ocean. Such multimodal eddies could affect the reconstructed vertical structure of the eddies. Second, the vertical mode is not always independent of the horizontal coordinates. The temperature dipole on the eddy surface (Figure 7; W.-Z. Zhang et al., 2018) and the tilting of the eddy axis (Z. Zhang et al., 2016) are observed in many studies, implying that the vertical mode varies in the eddy.

The eddy-induced transports could play an important role in the heat and fresh water budget, the water mass (e.g., SAMW) redistribution, and primary production in the southeastern Indian Ocean. The offshore volume transport by eddy drift across the coastal (107°W) section is 9.05 Sv (12.5 Sv). The heat and salt

onshore transport by eddy drift across the coastal (107°W) section are, respectively, 10.6 Tw and 143.1 ton/s (17.1 Tw and 241.0 ton/s). The heat and salt flux by eddy drift is comparable with the surface heat and freshwater flux and can influence the temperature and salinity variability of the LC and LUC. Moreover, the interannual temperature and salinity variations in SIO could be influenced by the eddy-induced heat and salt transports, whose interannual variability is pending for further studies.

Data Availability Statement

The Ssalto/Duacs altimeter products were produced and distributed by the Copernicus Marine and Environment Monitoring Service (CMEMS) (http://marine.copernicus.eu). Argo data were collected and made freely available by the International Argo Program and the national programs that contribute to it (ftp://ftp.ifremer.fr/ifremer/argo/geo/). OISST data were downloaded at the website (https://www.ncdc.noaa.gov/oisst/optimum-interpolation-sea-surface-temperature-oisst-v20). CARS09 mixed layer data are from the website (http://www.marine.csiro.au/~dunn/cars2009/).

Acknowledgment
This work was jointly supported by the Frontier Science Key Research Program of the Chinese Academy of Sciences (No. QYZDJ-SSW-DQC034), Grant No. GML2019ZD0304 from Southern Marine Science and Engineering Guangdong Laboratory (Guangzhou), NSFC Grants 41521005, 41776008, Youth Innovation Promotion Association CAS (2019336), the Guangzhou Science and Technology Program 201804010373, the Natural Science Foundation of Guangdong Province 2018A030313432, 2020A1515010361, Youth science and technology innovation talent of Guangdong TeZhi plan (2019TQ05H519), Pearl River S&T Nova Program of Guangzhou (201806010091), and the Open Project Program of State Key Laboratory of Tropical Oceanography (LTOZZ2002). Yinghui He was supported by the China Scholarship Council to visit the CSIRO. The data processing is supported by the High Performance Computing Division in the South China Sea Institute of Oceanology.

References

Amores, A., Melnichenko, O., & Maximenko, N. (2017). Coherent mesoscale eddies in the North Atlantic subtropical gyre: 3-D structure and transport with application to the salinity maximum. *Journal of Geophysical Research: Oceans*, *122*(1), 23–41. https://doi.org/10.1002/2016JC012256

Assassi, C., Morel, Y., Vandermeirsch, F., Chaigneau, A., Pegliasco, C., Morrow, R., et al. (2016). An index to distinguish surface- and subsurface-intensified vortices from surface observations. *Journal of Physical Oceanography*, *46*(8), 2529–2552. https://doi.org/10.1175/jpo-d-15-0122.1

Barceló-Llull, B., Sangrà, P., Pallàs-Sanz, E., Barton, E. D., Estrada-Allis, S. N., Martínez-Marrero, A., et al. (2017). Anatomy of a subtropical intrathermocline eddy. *Deep Sea Research Part I: Oceanographic Research Papers*, *124*, 126–139. https://doi.org/10.1016/j.dsr.2017.03.012

Capet, X., Colas, F., Mcwilliams, J. C., Penven, P., & Marchesiello, P. (2013). Eddies in eastern boundary subtropical upwelling systems. In M. W. Hecht & H. Hasumi (Eds.), *Ocean modeling in an eddying regime* (pp. 131–147). https://doi.org/10.1029/177gm10

Castelao, R. M. (2014). Mesoscale eddies in the South Atlantic bight and the Gulf Stream recirculation region: Vertical structure. *Journal of Geophysical Research: Oceans*, *119*(3), 2048–2065. https://doi.org/10.1002/2014JC009796

Chaigneau, A., Gizolme, A., & Grados, C. (2008). Mesoscale eddies off Peru in altimeter records: Identification algorithms and eddy spatio-temporal patterns. *Progress in Oceanography*, *79*(2–4), 106–119. https://doi.org/10.1016/j.pocean.2008.10.013

Chaigneau, A., Le Texier, M., Eldin, G., Grados, C., & Pizarro, O. (2011). Vertical structure of mesoscale eddies in the eastern South Pacific Ocean: A composite analysis from altimetry and Argo profiling floats. *Journal of Geophysical Research*, *116*(C11), C11025. https://doi.org/10.1029/2011jc007134

Chelton, D. B., Schlax, M. G., & Samelson, R. M. (2011). Global observations of nonlinear mesoscale eddies. *Progress in Oceanography*, *91*(2), 167–216. http://dx.doi.org/10.1016/j.pocean.2011.01.002

Chen, G., Hou, Y., & Chu, X. (2011). Mesoscale eddies in the South China Sea: Mean properties, spatiotemporal variability, and impact on thermohaline structure. *Journal of Geophysical Research*, *116*(C6), C06018. https://doi.org/10.1029/2010jc006716

Cheng, X., McCreary, J. P., Qiu, B., Qi, Y., Du, Y., & Chen, X. (2018). Dynamics of eddy generation in the Central Bay of Bengal. *Journal of Geophysical Research: Oceans*, *123*(9), 6861–6875. https://doi.org/10.1029/2018JC014100

Condie, S. A., & Dunn, J. R. (2006). Seasonal characteristics of the surface mixed layer in the Australasian region: Implications for primary production regimes and biogeography. *Marine Freshwater Research*, *57*(6), 569–590. https://doi.org/10.1071/MF06009

Cornuelle, B. D., Chereskin, T. K., Niiler, P. P., Morris, M. Y., & Musgrave, D. L. (2000). Observations and modeling of a California undercurrent eddy. *Journal of Geophysical Research*, *105*(C1), 1227–1243. https://doi.org/10.1029/1999jc900284

Cushman-Roisin, B., & J.-M. Beckers, (2011). Chapter 16—Quasi-geostrophic dynamics. In B. Cushman-Roisin & J.-M. Beckers (Eds.), *International geophysics* (pp. 521–551), Academic Press. https://doi.org/10.1016/B978-0-12-088759-0.00016-X

Czeschel, R., Schütte, F., Weller, R. A., & Stramma, L. (2018). Transport, properties, and life cycles of mesoscale eddies in the eastern tropical South Pacific. *Ocean Science*, *14*(4), 731–750. https://doi.org/10.5194/os-14-731-2018

Dilmahamod, A. F., Aguiar-González, B., Penven, P., Reason, C. J. C., De Ruijter, W. P. M., Malan, N., & Hermes, J. C. (2018). SIDDIES corridor: A major east-west pathway of long-lived surface and subsurface eddies crossing the subtropical South Indian Ocean. *Journal of Geophysical Research: Oceans*, *123*(8), 5406–5425. https://doi.org/10.1029/2018JC013828

Domingues, C. M., Wijffels, S. E., Maltrud, M. E., Church, J. A., & Tomczak, M. (2006). Role of eddies in cooling the Leeuwin Current. *Geophysical Research Letters*, *33*(5), L05603. https://doi.org/10.1029/2005GL025216

Dong, D., Brandt, P., Chang, P., Schütte, F., Yang, X., Yan, J., & Zeng, J. (2017). Mesoscale eddies in the Northwestern Pacific Ocean: Three-dimensional eddy structures and heat/salt transports. *Journal of Geophysical Research: Oceans*, *122*(12), 9795–9813. https://doi.org/10.1002/2017JC013303

Dufois, F., Hardman-Mountford, N. J., Greenwood, J., Richardson, A. J., Feng, M., Herbette, S., & Matear, R. (2014). Impact of eddies on surface chlorophyll in the South Indian Ocean. *Journal of Geophysical Research: Oceans*, *119*(11), 8061–8077. https://doi.org/10.1002/2014JC010164

Early, J. J., Samelson, R. M., & Chelton, D. B. (2011). The evolution and propagation of quasigeostrophic ocean eddies. *Journal of Physical Oceanography*, *41*, 1535–1555. https://doi.org/10.1175/2011JPO4601.1

Faghmous, J. H., Frenger, I., Yao, Y., Warmka, R., Lindell, A., & Kumar, V. (2015). A daily global mesoscale ocean eddy dataset from satellite altimetry. *Scientific Data*, *2*, 150028. https://doi.org/10.1038/sdata.2015.28

Feng, M., Majewski, L. J., Fandry, C. B., & Waite, A. M. (2007). Characteristics of two counter-rotating eddies in the Leeuwin current system off the Western Australian coast. *Deep Sea Research Part II: Topical Studies in Oceanography*, *54*(8–10), 961–980. http://doi.org/10.1016/j.dsr2.2006.11.022

Feng, M., Meyers, G., Pearce, A., & Wijffels, S. (2003). Annual and interannual variations of the Leeuwin Current at 32°S. *Journal of Geophysical Research*, *108*(C11). https://doi.org/10.1029/2002JC001763

Feng, M., Wijffels, S., Godfrey, S., & Meyers, G. (2005). Do eddies play a role in the momentum balance of the Leeuwin current? *Journal of Physical Oceanography*, *35*(6), 964–975. https://doi.org/10.1175/JPO2730.1

Fieux, M., Molcard, R., & Morrow, R. (2005). Water properties and transport of the Leeuwin Current and eddies off Western Australia. *Deep Sea Research Part I: Oceanographic Research Papers*, *52*(9), 1617–1635. https://doi.org/10.1016/j.dsr.2005.03.013

Flierl, G. R. (1981). Particle motions in large-amplitude wave fields. *Geophysical & Astrophysical Fluid Dynamics*, *18*(1–2), 39–74. https://doi.org/10.1080/03091928108208773

Flierl, G. R. (1987). Isolated Eddy models in geophysics. *Annual Review of Fluid Mechanics*, *19*(1), 493–530. https://doi.org/10.1146/annurev.fl.19.010187.002425

Furue, R. (2019). The three-dimensional structure of the Leeuwin current system in density coordinates in an eddy-resolving OGCM. *Ocean Modelling*, *138*, 36–50. https://doi.org/10.1016/j.ocemod.2019.03.001

Furue, R., Guerreiro, K., Phillips, H. E., McCreary, J. P., & Bindoff, N. L. (2017). On the Leeuwin current system and its linkage to zonal flows in the South Indian Ocean as inferred from a gridded hydrography. *Journal of Physical Oceanography*, *47*(3), 583–602. https://doi.org/10.1175/jpo-d-16-0170.1

Gaube, P., Chelton, D. B., Samelson, R. M., Schlax, M. G., & O'Neill, L. W. (2015). Satellite observations of mesoscale Eddy-induced Ekman pumping. *Journal of Physical Oceanography*, *45*(1), 104–132. https://doi.org/10.1175/jpo-d-14-0032.1

Gulakaram, V. S., Vissa, N. K., & Bhaskaran, P. K. (2020). Characteristics and vertical structure of oceanic mesoscale eddies in the Bay of Bengal. *Dynamics of Atmospheres and Oceans*, *89*, 101131. https://doi.org/10.1016/j.dynatmoce.2020.101131

Guo, Y., Li, Y., Wang, F., Wei, Y., & Rong, Z. (2020). Processes controlling sea surface temperature variability of Ningaloo Niño. *Journal of Climate*, *33*(10), 4369–4389. https://doi.org/10.1175/jcli-d-19-0698.1

Guo, Y., Li, Y., Wang, F., Wei, Y., & Xia, Q. (2020). Importance of resolving mesoscale eddies in the model simulation of Ningaloo Niño. *Geophysical Research Letters*, *47*(14), e2020GL087998. https://doi.org/10.1029/2020GL087998

Hausmann, U., & Czaja, A. (2012). The observed signature of mesoscale eddies in sea surface temperature and the associated heat transport. *Deep Sea Research Part I: Oceanographic Research Papers*, *70*(Supplement C), 60–72. https://doi.org/10.1016/j.dsr.2012.08.005

He, Q., Zhan, H., Cai, S., He, Y., Huang, G., & Zhan, W. (2018). A new assessment of mesoscale eddies in the South China Sea: Surface features, three-dimensional structures, and thermohaline transports. *Journal of Geophysical Research: Oceans*, *123*(7), 4906–4929. https://doi.org/10.1029/2018JC014054

He, Y., Feng, M., Xie, J., Liu, J., Chen, Z., Xu, J., et al. (2017). Spatiotemporal variations of mesoscale eddies in the Sulu Sea. *Journal of Geophysical Research: Oceans*, *122*(10), 7867–7879. https://doi.org/10.1002/2017JC013153

He, Y., Xie, J., & Cai, S. (2016). Interannual variability of winter eddy patterns in the eastern South China Sea. *Geophysical Research Letters*, *43*(10), 5185–5193. https://doi.org/10.1002/2016GL068842

Hormazabal, S., Combes, V., Morales, C. E., Correa-Ramirez, M. A., Di Lorenzo, E., & Nuñez, S. (2013). Intrathermocline eddies in the coastal transition zone off central Chile (31-41°S). *Journal of Geophysical Research: Oceans*, *118*(10), 4811–4821. https://doi.org/10.1002/jgrc.20337

Keppler, L., Cravatte, S., Chaigneau, A., Pegliasco, C., Gourdeau, L., & Singh, A. (2018). Observed characteristics and vertical structure of mesoscale eddies in the Southwest Tropical Pacific. *Journal of Geophysical Research: Oceans*, *123*(4), 2731–2756. https://doi.org/10.1002/2017JC013712

Kurian, J., Colas, F., Capet, X., McWilliams, J. C., & Chelton, D. B. (2011). Eddy properties in the California current system. *Journal of Geophysical Research*, *116*(C8), C08027. https://doi.org/10.1029/2010jc006895

Li, Q.-Y., Sun, L., & Lin, S.-F. (2016). GEM: A dynamic tracking model for mesoscale eddies in the ocean. *Ocean Science*, *12*(6), 1249–1267. https://doi.org/10.5194/os-12-1249-2016

Locarnini, R. A., Mishonov, A. V., Antonov, J. I., Boyer, T. P., Garcia, H. E., Baranova, O. K., et al. (2013). World Ocean Atlas 2013, volume 1: Temperature. In S. Levitus, & A. Mishonov Technical (Eds.), NOAA atlas NESDIS (73, p. 40).

Mao, H., Feng, M., Phillips, H. E., & Lian, S. (2018). Mesoscale eddy characteristics in the interior subtropical southeast Indian Ocean, tracked from the Leeuwin Current system. *Deep Sea Research Part II: Topical Studies in Oceanography*. https://doi.org/10.1016/j.dsr2.2018.07.003

McGillicuddy, D. J., Anderson, L. A., Bates, N. R., Bibby, T., Buesseler, K. O., Carlson, C. A., et al. (2007). Eddy/wind interactions stimulate extraordinary mid-ocean plankton blooms. *Science*, *316*(5827), 1021–1026. https://doi.org/10.1126/science.1136256

Menezes, V. V., Phillips, H. E., Schiller, A., Bindoff, N. L., Domingues, C. M., & Vianna, M. L. (2014). South Indian countercurrent and associated fronts. *Journal of Geophysical Research: Oceans*, *119*(10), 6763–6791. https://doi.org/10.1002/2014jc010076

Menezes, V. V., Phillips, H. E., Vianna, M. L., & Bindoff, N. L. (2016). Interannual variability of the South Indian Countercurrent. *Journal of Geophysical Research: Oceans*, *121*(5), 3465–3487. https://doi.org/10.1002/2015jc011417

Moore, T. S., Matear, R. J., Marra, J., & Clementson, L. (2007). Phytoplankton variability off the Western Australian Coast: Mesoscale eddies and their role in cross-shelf exchange. *Deep Sea Research Part II: Topical Studies in Oceanography*, *54*(8), 943–960. http://doi.org/10.1016/j.dsr2.2007.02.006

Morrow, R., Birol, F., Griffin, D., & Sudre, J. (2004). Divergent pathways of cyclonic and anti-cyclonic ocean eddies. *Geophysical Research Letters*, *31*(24), L24311. https://doi.org/10.1029/2004GL020974

Morrow, R., Fang, F., Fieux, M., & Molcard, R. (2003). Anatomy of three warm-core Leeuwin current eddies. *Deep Sea Research Part II: Topical Studies in Oceanography*, *50*(12–13), 2229–2243. https://doi.org/10.1016/S0967-0645(03)00054-7

Pearce, A. F., & Griffiths, R. W. (1991). The mesoscale structure of the Leeuwin current: A comparison of laboratory models and satellite imagery. *Journal of Geophysical Research*, *96*(C9), 16739–16757. https://doi.org/10.1029/91JC01712

Pegliasco, C., Chaigneau, A., & Morrow, R. (2015). Main eddy vertical structures observed in the four major Eastern Boundary Upwelling Systems. *Journal of Geophysical Research: Oceans*, *120*(9), 6008–6033. https://doi.org/10.1002/2015JC010950

Pelland, N. A., Eriksen, C. C., & Lee, C. M. (2013). Subthermocline eddies over the Washington continental slope as observed by seagliders, 2003-09. *Journal of Physical Oceanography*, *43*(10), 2025–2053. https://doi.org/10.1175/jpo-d-12-086.1

Qu, T., Lian, Z., Nie, X., & Wei, Z. (2019). Eddy-induced meridional salt flux and its impacts on the sea surface salinity maxima in the Southern Subtropical oceans. *Geophysical Research Letters*, *46*(20), 11292–11300. https://doi.org/10.1029/2019gl084807

Rennie, S. J., Pattiaratchi, C. P., & McCauley, R. D. (2007). Eddy formation through the interaction between the Leeuwin current, Leeuwin undercurrent and topography. *Deep Sea Research Part II: Topical Studies in Oceanography*, *54*(8), 818–836. https://doi.org/10.1016/j.dsr2.2007.02.005

Steinberg, J. M., Pelland, N. A., & Eriksen, C. C. (2019). Observed evolution of a California undercurrent eddy. *Journal of Physical Oceanography*, *49*(3), 649–674. https://doi.org/10.1175/jpo-d-18-0033.1

Sun, B., Liu, C., & Wang, F. (2019). Global meridional eddy heat transport inferred from Argo and altimetry observations. *Scientific Reports*, *9*(1), 1345. https://doi.org/10.1038/s41598-018-38069-2

Sun, W., Dong, C., Wang, R., Liu, Y., & Yu, K. (2017). Vertical structure anomalies of oceanic eddies in the Kuroshio extension region. *Journal of Geophysical Research: Oceans*, *122*(2), 1476–1496. https://doi.org/10.1002/2016JC012226

Talley, L. D., Pickard, G. L., Emery, W. J., & Swift, J. H. (2011). Chapter 11—Indian Ocean. In L. D. Talley, G. L. Pickard, W. J. Emery & J. H. Swift (Eds.), (Eds), *Descriptive physical oceanography* (6th ed., pp. 363–399). Boston: Academic Press. https://doi.org/10.1016/B978-0-7506-4552-2.10011-3

Waite, A. M., Thompson, P. A., Pesant, S., Feng, M., Beckley, L. E., Domingues, C. M., et al. (2007). The Leeuwin Current and its eddies: An introductory overview. *Deep Sea Research Part II: Topical Studies in Oceanography*, *54*(8–10), 789–796. http://doi.org/10.1016/j.dsr2.2006.12.008

Woo, M., & Pattiaratchi, C. (2008). Hydrography and water masses off the western Australian coast. *Deep Sea Research Part I: Oceanographic Research Papers*, *55*(9), 1090–1104. https://doi.org/10.1016/j.dsr.2008.05.005

Yang, G., Wang, F., Li, Y., & Lin, P. (2013). Mesoscale eddies in the northwestern subtropical Pacific Ocean: Statistical characteristics and three-dimensional structures. *Journal of Geophysical Research: Oceans*, *118*(4), 1906–1925. https://doi.org/10.1002/jgrc.20164

Yang, G., Yu, W., Yuan, Y., Zhao, X., Wang, F., Chen, G., et al. (2015). Characteristics, vertical structures, and heat/salt transports of mesoscale eddies in the southeastern tropical Indian Ocean. *Journal of Geophysical Research: Oceans*, *120*(10), 6733–6750. https://doi.org/10.1002/2015JC011130

Zhang, W.-Z., Ni, Q., & Xue, H. (2018). Composite eddy structures on both sides of the Luzon Strait and influence factors. *Ocean Dynamics*, *68*(11), 1527–1541. https://doi.org/10.1007/s10236-018-1207-z

Zhang, Z., Li, P., Xu, L., Li, C., Zhao, W., Tian, J., & Qu, T. (2015). Subthermocline eddies observed by rapid-sampling Argo floats in the subtropical northwestern Pacific Ocean in Spring 2014. *Geophysical Research Letters*, *42*(15), 6438–6445. https://doi.org/10.1002/2015gl064601

Zhang, Z., Tian, J., Qiu, B., Zhao, W., Chang, P., Wu, D., & Wan, X. (2016). Observed 3D structure, generation, and dissipation of oceanic mesoscale eddies in the South China Sea. *Scientific Reports*, *6*, 11. https://doi.org/10.1038/srep24349

Zhang, Z., Wang, W., & Qiu, B. (2014). Oceanic mass transport by mesoscale eddies. *Science*, *345*(6194), 322–324. https://doi.org/10.1126/science.1252418

Zhang, Z., Zhang, Y., Wang, W., & Huang, R. X. (2013). Universal structure of mesoscale eddies in the ocean. *Geophysical Research Letters*, *40*(14), 3677–3681. https://doi.org/10.1002/grl.50736

Zheng, S., Du, Y., Li, J., & Cheng, X. (2015). Eddy characteristics in the South Indian Ocean as inferred from surface drifters. *Ocean Science*, *11*(3), 361–371. https://doi.org/10.5194/os-11-361-2015

Zheng, S., Feng, M., Du, Y., Meng, X., & Yu, W. (2018). Interannual variability of eddy kinetic energy in the subtropical Southeast Indian Ocean associated with the El Niño-Southern oscillation. *Journal of Geophysical Research: Oceans*, *123*(2), 1048–1061. https://doi.org/10.1002/2017JC013562

Zweng, M. M., Reagan, J. R., Antonov, J. I., Locarnini, R. A., Mishonov, A. V., Boyer, T. P., et al. (2013). World Ocean Atlas 2013, volume 2: Salinity. In S. Levitus, & A. Mishonov Technical (Eds.), NOAA atlas NESDIS (74, p. 39).